Pacific Northwest
NATIONAL LABORATORY

PNNL-29814

Mid-Atlantic Bight Wave Hindcast to Support DOE Lidar Buoy Deployments: Model Validation

April 2020

Gabriel García Medina
William Shaw
Zhaoqing Yang
Rob Newsom

U.S. DEPARTMENT OF ENERGY

Prepared for the U.S. Department of Energy
under Contract DE-AC05-76RL01830

PACIFIC NORTHWEST NATIONAL LABORATORY
operated by
BATTELLE
for the
UNITED STATES DEPARTMENT OF ENERGY
under Contract DE-AC05-76RL01830

Printed in the United States of America

Available to DOE and DOE contractors from the
Office of Scientific and Technical Information,
P.O. Box 62, Oak Ridge, TN 37831-0062;
ph: (865) 576-8401
fax: (865) 576-5728
email: reports@adonis.osti.gov

Available to the public from the National Technical Information Service
5301 Shawnee Rd., Alexandria, VA 22312
ph: (800) 553-NTIS (6847)
email: orders@ntis.gov <https://www.ntis.gov/about>
Online ordering: http://www.ntis.gov

PNNL-29814

Mid-Atlantic Bight Wave Hindcast to Support DOE Lidar Buoy Deployments: Model Validation

April 2020

Gabriel García Medina
William Shaw
Zhaoqing Yang
Rob Newsom

Prepared for
the U.S. Department of Energy
under Contract DE-AC05-76RL01830

Pacific Northwest National Laboratory
Richland, Washington 99354

Abstract

This study presents a shelf-scale wave hindcast for the Mid-Atlantic Bight to provide accurate wave data that complements the data gathered by two U.S. Department of Energy Lidar buoy deployments off the coasts of Virginia and New Jersey, respectively. Pacific Northwest National Laboratory developed an approximately 2 km resolution model based on the WAVEWATCH III model that was forced with analyzed winds and ocean currents, as well as executed a 4-year hindcast for the period from January 2014 to December 2017. The model results compared well against 16 wave-measuring buoys and data derived from six satellite-borne radar altimeters. In addition, the model results for two storm events that generated large waves, Hurricane Hermine and the January 2016 U.S. blizzard, are discussed in detail.

Acknowledgments

This work was supported by the Wind Energy Technologies Office of the U.S. Department of Energy's Office of Energy Efficiency and Renewable Energy. The model computations were performed using resources available through Research Computing at Pacific Northwest National Laboratory (PNNL). PNNL is operated by Battelle for the U.S. Department of Energy under Contract DE-AC05-76RL01830. Mikhail Pekour (PNNL) made the initial quality checks and data extraction from the TRIAXYS dataset. The authors acknowledge Fadia Marion Ticona Rollano (PNNL) for processing data from the National Data Buoy Center.

Acronyms and Abbreviations

CFSRv2	Climate Forecast System Reanalysis Version 2
CSI	Coastal Studies Institute
DMME	Department of Mines, Minerals, and Energy
DOE	U.S. Department of Energy
Hz	hertz
HYCOM	HYbrid Coordinate Ocean Model
km	kilometer(s)
kW/m	kilowatt(s) per meter
m	meter(s)
NDBC	National Data Buoy Center
PE	percentage error
PNNL	Pacific Northwest National Laboratory
R	correlation coefficient
R_θ	angular correlation coefficient
RMSE	root-mean-square error
s	second(s)
SI	scatter index
SIO	Scrips Institution of Oceanography
SWAN	Simulating WAves Nearshore
TB	terabyte(s)
USACE	U.S. Army Corps of Engineers
WW3	WAVEWATCH III
yr	year(s)

Contents

Figures

Tables

1.0 Introduction

Pacific Northwest National Laboratory operated two AXYS WindSentinel Lidar buoys in the Atlantic Ocean off the coasts of Virginia and New Jersey for the U.S. Department of Energy (DOE) between 2014 and 2017. The centerpiece of these systems is a Doppler Lidar instrument that measures the vector wind velocity in 40 m height increments from approximately 40 m to 200 m above the sea surface (Shaw et al. 2018). In addition to the wind profile, the buoy systems also measured a variety of supporting meteorological and oceanographic information, including sea state in the form of the two-dimensional wave spectrum.

Wind stress over the ocean depends in part on the sea state (e.g., Drennan et al. 2005; Pan et al. 2005), where the misalignment between the swell and wind can affect the stress magnitude and direction (Drennan et al. 1999). When swells travel faster than wind, they can transfer momentum from the ocean to the atmosphere (Grachev and Fairall 2001). The study of a coupled system such as this one is an area of active research that the DOE buoys are well suited to support.

A commonly used surface roughness length scale for atmospheric models that considers the wind-driven surface gravity wave effects proposed by Taylor and Yelland (2001) is:

$$\frac{z_0}{H_{m0}} = A\left(\frac{H_{m0}}{L_p}\right)^B \tag{1.1}$$

where z_0 is the surface roughness length scale, H_{m0} is the significant wave height, L_p is the wavelength of the most energetic component of the sea state, and A and B are empirical coefficients. Wave conditions are variable in time and space; the former can be captured with in situ measurements at high sampling rates, while the latter requires spatial coverage able to resolve variations in the wave field.

Even though the continental shelf off the East Coast of the U.S. is well monitored with respect to other areas of the world, the buoy network is still too sparse to get a full picture of the wave transformations across the shelf. During the 4-year period from 2014 to 2017, 16 buoys were deployed in the Mid-Atlantic Bight shelf by many federal and state agencies, including the two DOE Lidar buoys. The timeframes of these measurements did not fully overlap, and data gaps exist in their records. To provide full spatial and temporal wave information needed for the surface boundary conditions for atmospheric models, it is necessary to use a wave model. When the wave model is executed for past conditions, the wave modeling produces what is termed a “hindcast.”

Shaw et al. (2020) provides a general analysis of the conditions during the Lidar buoy deployments, including details of the development of a high-resolution (~2 km spatial resolution) wind-driven surface gravity wave model (“wave model” hereafter). This model was developed based on the state-of-the-art WAVEWATCH III (WW3) model that is particularly useful for simulations over the continental shelf. The report herein describes the model setup and application for producing a high-resolution hindcast for the Mid-Atlantic Bight, as well as its validation against in situ and satellite-based remote measurements.

2.0 Model Setup

The third-generation, phase-averaged model WW3 v5.16 (Tolman and WAVEWATCH III Development Group (2014)) is being implemented to dynamically downscale waves over the Mid-Atlantic Bight. The area covered by the model is shown in Figure 2.1. The modeling system consists of four levels that increase in resolution from a 30 arc-minute resolution global model (L1) to a high-resolution 1.2 arc-minute shelf-scale model (L4). The L4 model extends past the shelf break to simulate the wave transformations as they enter intermediate waters. The model is forced with analyzed global winds at a height of 10 m from the Climate Forecast System Reanalysis Version 2 (CFSRv2; Saha et al. (2014)) and analyzed surface currents from the HYbrid Coordinate Ocean Model (HYCOM) (Halliwell 2004). Further details of the model setup, development, and sensitivity analysis can be found in Shaw et al. (2020).

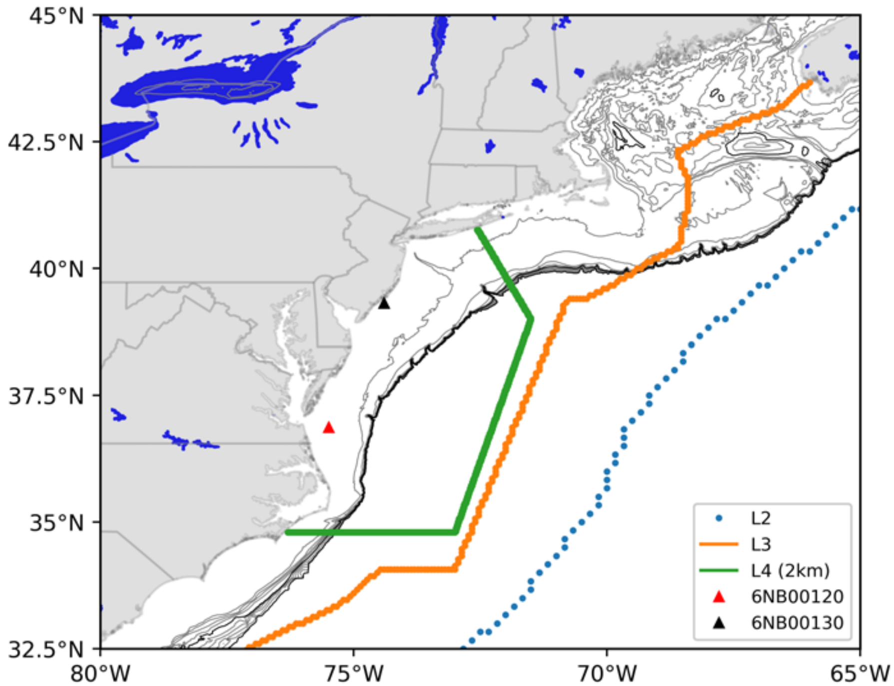

Figure 2.1. Extents of the model system with respect to the Lidar buoys. Bathymetry contours are shown between 50 and 500 m with a 50 m interval. The DOE Lidar buoys off the coasts of Virginia and New Jersey are shown as red and black triangles, respectively.

WW3 solves the spectral wave action balance equation:

$$\frac{\partial N}{\partial t}+\frac{\partial c_{gx}N}{\partial x}+\frac{\partial c_{gy}N}{\partial y}+\frac{\partial c_{k}N}{\partial k}+\frac{\partial c_{\theta}N}{\partial \theta}=\frac{1}{\sigma}\left(S_{in}+S_{ds}+S_{nl}+S_{bot}+S_{brk}\right)=S_{tot} \tag{2.1}$$

where $N(t,x,y,k,\theta)=\frac{F(k,\theta)}{\sigma}$ is the wave action, F is the wavenumber and directionally resolved variance spectrum, t is time, x and y are the position, c is the velocity of propagation in each dimension, σ is the radian frequency, θ is the direction, k is the wave number, and S_{tot} is the combined effect of the sinks and sources of energy that transform the waves. These combined effects include wave growth (S_{in}), dissipation due to whitecapping (S_{ds}), nonlinear quadruplet interactions (S_{nl}), dissipation due to bottom friction (S_{bot}), and depth-induced wave breaking (S_{brk}). Since WW3 is based on linear wave theory, the wave number and radian frequency are related by the linear dispersion relation:

$$\sigma^2 = gk \tanh kh, \tag{2.2}$$

where h is the water depth. At any given point in time and space, the frequency and direction spectrum (E) can be obtained by

$$E = \frac{2\pi}{c_g} F, \tag{2.3}$$

where c_g is the group velocity. The significant wave height (H_{m0}) can be estimated from the frequency spectrum as:

$$H_{m0} = 4\sqrt{m_0}, \tag{2.4}$$

where the spectral moments are defined by $m_n = \int \sigma^n E(\sigma) d\sigma$. The peak wave period ($T_p$) is the inverse of the frequency that has maximum energy from the directionally integrated spectrum. The average wave period (T_a) is defined from the second spectral moment:[1]

$$T_a = \sqrt{\frac{m_0}{m_2}}. \tag{2.5}$$

T_a was found to correspond well to the average wave period obtained from a time domain analysis of water surface elevation. The peak wave direction (D_p) is computed in a similar way to T_p but using the frequency integrated spectra. Finally, similar to the T_a, the vector mean wave direction (D_a) provides a spectrally weighted mean direction of propagation. Following Kuik et al. (1988), D_a is defined as:

$$D_a = \tan^{-1} \frac{\int E(\sigma) b_1(\sigma) d\sigma}{\int E(\sigma) a_1(\sigma) d\sigma}, \tag{2.6}$$

where a_1 and b_1 are the first two directional Fourier coefficients (Longuet-Higgins et al. 1963). The first four directional Fourier coefficients are given by:

$$\begin{aligned} a_1 &= \int E(f,\theta) \cos\theta \, d\theta \\ b_1 &= \int E(f,\theta) \sin\theta \, d\theta \\ a_2 &= \int E(f,\theta) \cos 2\theta \, d\theta \\ b_2 &= \int E(f,\theta) \sin 2\theta \, d\theta \end{aligned} \tag{2.7}$$

Equation (2.6) could have been written in terms of the frequency and directional spectra but, as will be discussed in Section 3.1, these same Fourier coefficients are derived from the onboard sensors in the buoy deployments.

[1] T_a is also referred to as T_{m02} in the literature.

3.0 Data Sources

The measurements used to validate the model after the calibration period are discussed in this section, and the model calibration is discussed in Shaw et al. (2020). A combination of in situ and altimetry-based measurements are used in the analysis to provide a comprehensive characterization of the model performance.

3.1 DOE Lidar Buoy Measurements

The wave measurement from the Lidar buoy deployments off New Jersey (6NB00130) and Virginia (6NB00120) serve as source ground truth data for the wave model. The Lidar buoys are equipped with TRIAXYS Next Wave II sensors that record the movements of the floating platform from which wave height, wave period, and wave direction are estimated. The TRIAXYS system incorporates an inertial sensor that provides measurements of pitch, roll, three components of angular rate, and three components of acceleration relative to the buoy's frame of reference. The TRIAXYS system also contains a flux gate compass that provides a magnetic heading reference so that the accelerations and velocities can be transformed to an Earth-fixed frame of reference. After correction for the mooring response, estimates of wave slope, heave displacement, and sway and surge velocities are computed using the inertial data.

The AXYS wave analysis algorithm first performs a so-called "zero-crossing analysis" of the heave displacement data to estimate the average, significant, and maximum wave heights, as well as the average wave period. The non-directional wave spectrum is computed in the frequency domain after performing a Fourier transform of the wave elevation (heave displacement) data.

A preliminary directional wave analysis is performed using a modified version of the KVH method (Kuik et al. 1988). The various cross spectra of the heave displacement with the east-west velocity components are computed, from which the first four Fourier coefficients $a_1(f)$, $b_1(f)$, $a_2(f)$, and $b_2(f)$ of the directional spreading function (Steele et al. 1992) are obtained. These coefficients are then used to compute the mean wave direction and the directional spreading width as functions of frequency. A final directional wave analysis is then performed using the maximum entropy method (Nwogu et al. 1987) to obtain the directional wave spectrum.

3.2 In Situ Measurements

There are 14 buoys inside the L4 domain that are owned and operated by different agencies (Table 3.1) in addition to the DOE lidar buoys. These buoys provide coverage over the shelf, as shown in Figure 3.1, providing the basis for model-data comparisons. The buoys are located in shallow to intermediate water depths—depending on the incident wave period—from 8 to 78 m (Table 3.1).

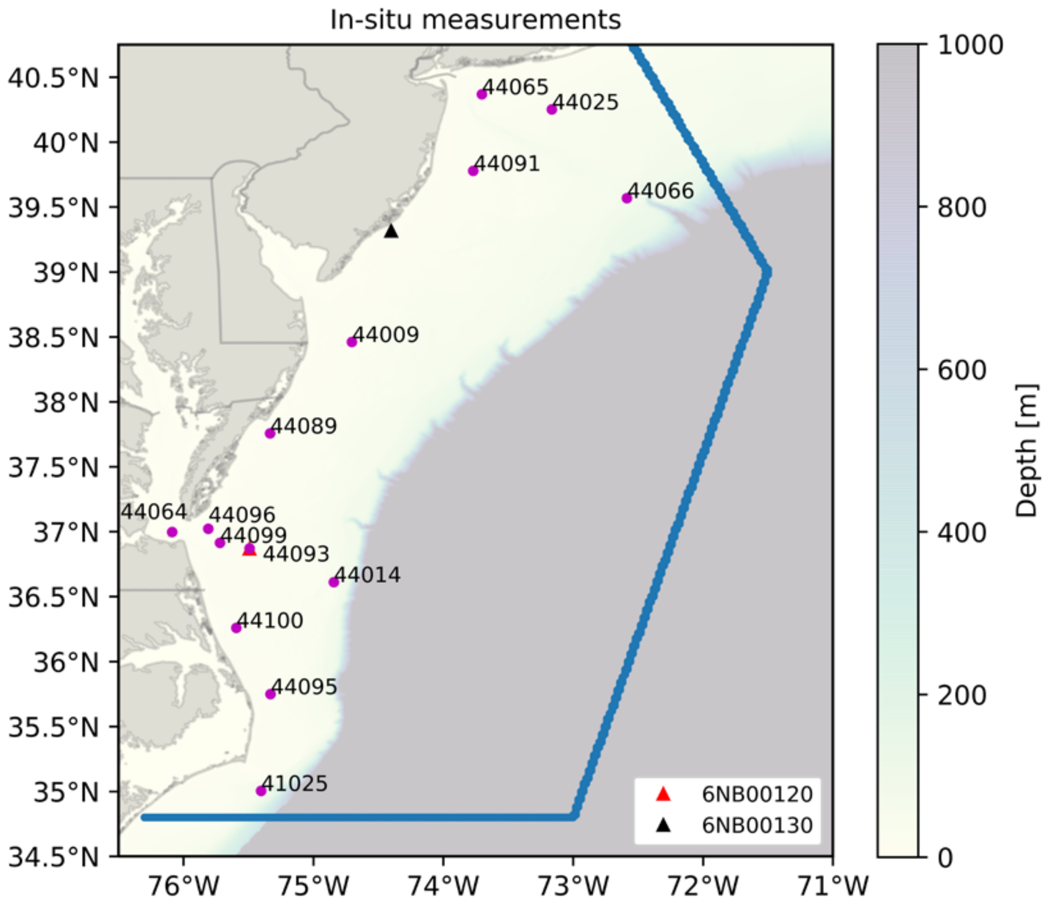

Figure 3.1. Location of wave buoys used for model validation with National Data Buoy Center (NDBC) identifiers. DOE Lidar buoys are also shown as triangles. Note that 44093 and 6NB00120 are located within 600 m from each other.

Table 3.1. Buoys used for model validation. These are owned and maintained by the NDBC, the Chesapeake Bay Interpretative Buoy System (CBIBS), U.S. Army Corps of Engineers (USACE), Virginia Department of Mines, Minerals, and Energy (DMME), Coastal Studies Institute (CSI), and Scrips Institution of Oceanography (SIO).

ID	Agency	Depth [m]	Operation Period
41025	NDBC	59	2003–present
44009	NDBC	30	1984–present
44014	NDBC/USACE	47	1990–present
44025	NDBC	36	1975–present
44064	CBIBS	8	2011–present
44065	NDBC	25	2008–present
44066	NDBC	78	2009–present
44089	USACE	17	2016–present
44091	USACE	26	2014–present
44093	DMME	27	2014–2017
44095	CSI	18	2012–present
44096	SIO	12	2012–2018
44099	SIO	18	2008–present
44100	SIO	26	2008–present

NDBC buoys equipped with motion sensors do not transmit the time series of measurements to shore. Instead, they transform the measurements to the frequency domain via Fourier transform and transmit the information shoreward.[1] Thus, the spectral properties of the waves are estimated from the frequency domain and are not direct measurements. Consequently, the bulk wave parameters are obtained in the same way the model-derived parameters are obtained (see Section 2.0).

3.3 Satellite Altimetry

Altimetry-derived wave heights from satellites provide global spatial coverage (Young and Donelan 2018) with an accuracy comparable to the buoy measurements. During the deployment period, there were six altimeters that provided significant wave height estimates: JASON-2, JASON-3, SENTINEL-3A, HY-2, CRYOSAT-2, and SARAL. The data are obtained from the calibrated data set of Ribal and Young (2019) and the coverage period shown in Table 3.2. Altimeters only provide significant wave height; thus, for characterization of other properties of the wave field, such as periods and directions, in situ measurements are relied on.

[1] https://www.ndbc.noaa.gov/wave.shtml

Table 3.2. Altimeter repeat cycle and operation period.

Altimeter	Repeat Cycle [days]	Operation Period
JASON-2	10	2008–2019
CRYOSAT-2	30	2010–present
HY-2	14	2011–present
SARAL	35	2013–present
JASON-3	10	2016–present
SENTINEL-3A	27	2016–present

Wave height is obtained by analyzing the time of arrival of radar pulses which vary depending on which part of the wave (e.g., crest, trough) the pulse bounced from. These data are averaged over a certain distance to obtain a statistical representation of the sea state to obtain significant wave height. These values are usually calibrated against in situ buoy measurements (Carter et al. 1992).

4.0 Model Validation

A combination of in situ and altimeter observations are used to provide spatial and temporal characterization of the model errors during the hindcast period. Metrics for model validation of significant wave height and period used in this study are described in Appendix A.

4.1 Altimetry-Based Comparison

Altimeter swaths are narrow and essentially provide one point in the along-track direction. Thus, comparing the model against the altimetry-derived measurements tests the model for accurate magnitude and timing of the waves. Figure 4.1 and Figure 4.2 show direct comparisons of H_{mo} between JASON-2 and the WW3 model. The first figure shows a case of good agreement in the gradients, while the second shows a case with the model both overpredicting and underpredicting the waves. Both cases show typical results where the measurements have shorter-scale spatial variability that the model does not reproduce.

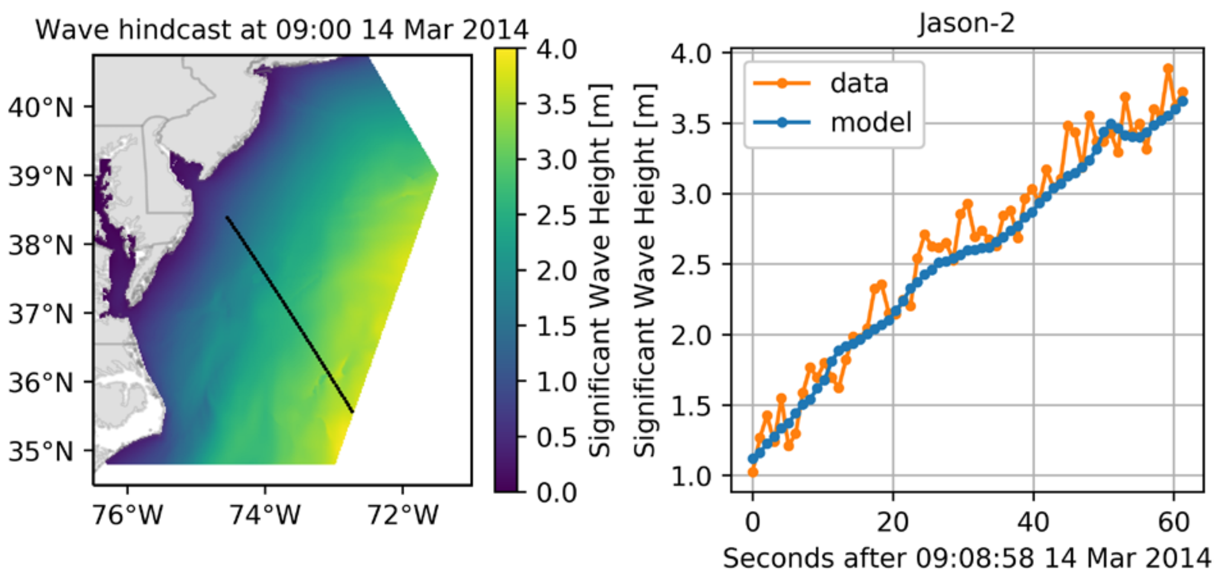

Figure 4.1. Direct comparison between the simulated waves and JASON-2 altimeter-derived waves. (*Left*) Altimeter tracks overlaid on a spatial snapshot of significant wave height. (*Right*) Along-track comparison of significant wave height, where the model results have been interpolated in time and space to the altimeter measurements.

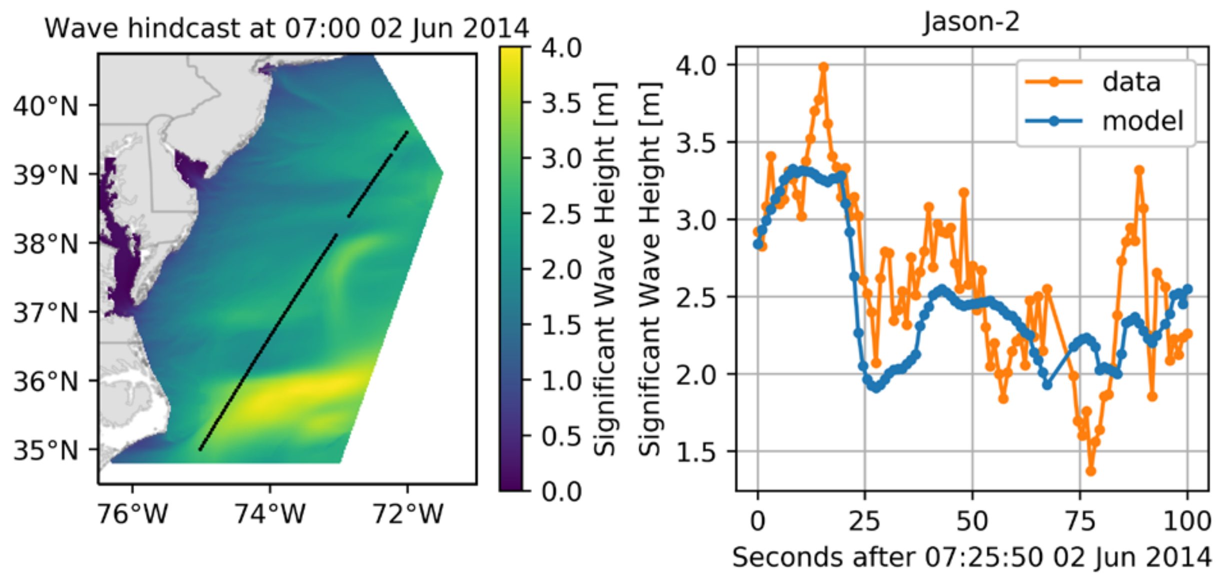

Figure 4.2. Same as Figure 4.1 but for a different period and track.

Model results were interpolated in time and space to match the measurements. The data were then binned in 0.2° by 0.2° cells to increase the number of points when computing error statistics and to aid visualization; at 40°N, this corresponds to 22.2 by 17.0 km bins. Root-mean-square error (RMSE), bias, and linear correlation coefficients are shown in Figure 4.3. RMSE is on average 0.42 m, with smaller errors in the nearshore. Overall, the model results are biased high by 0.17 cm. No clear spatial patterns in bias are observed in the model. Note that error statistics inside Chesapeake Bay are not representative of the model errors because tides and freshwater flows were not considered.

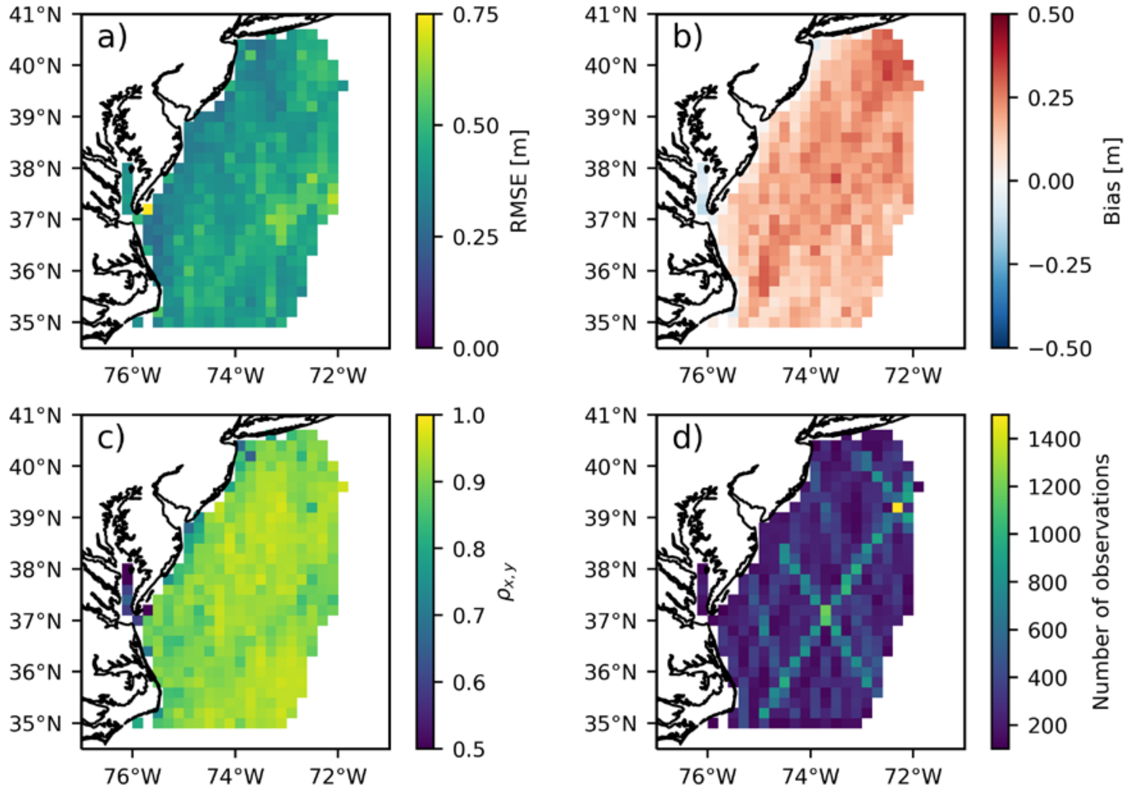

Figure 4.3. (a) RMSE, (b) bias, (c) linear correlation coefficient, and (d) number of observations in each bin for significant wave height comparisons.

4.2 Buoy-based Comparison: Wave Height and Period

This section describes the model errors from the perspective of total energy using significant wave height and its distribution in frequency space using different periods. To get a graphic idea of the general model performance, scatter plots were computed for Virginia and New Jersey deployments as shown in Figure 4.4 and Figure 4.5, respectively. In general, the distributions of H_{mo} are narrow (panel a) and the dominant sea states (hotter colors) are simulated accurately. The difference between the model hindcast and the observations increases for the largest events. Some of these events will be discussed in Section 4.4. T_p shows significantly larger scatter (panel b). This is not unexpected given that bimodal seas with comparable energy will make this statistic very scattered. Nevertheless, the most common sea states are captured accurately. On the other hand, T_a mitigates that behavior by using integrated spectral quantities (see panel c). The scatter is reduced with respect to the peak period, and again the hindcast is able to accurately reproduce the most common sea states as well as the cases when periods are longer. Scatter plots for the rest of the buoys are shown in Appendix B.

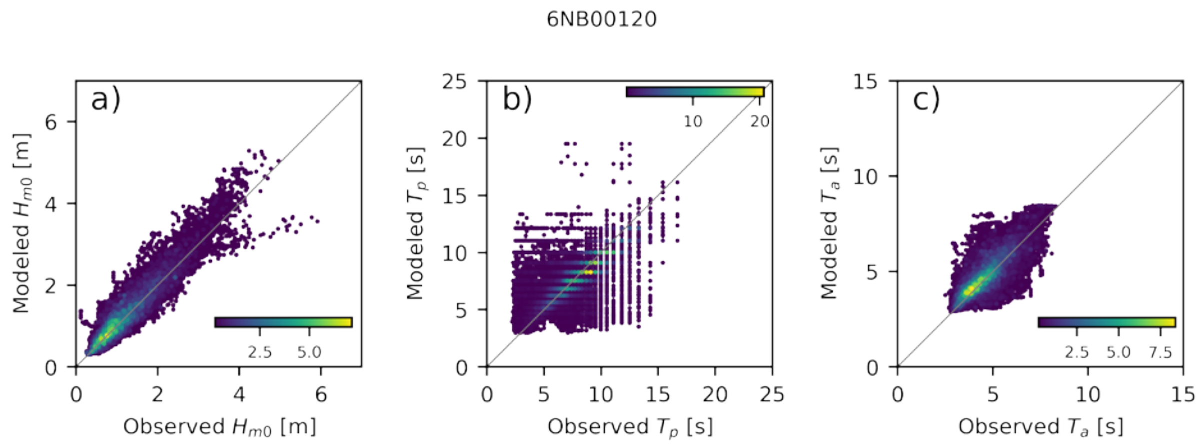

Figure 4.4. Scatter plots for (a) significant wave height, (b) peak wave period, and (c) mean wave period for the Virginia deployment. The colors show density of the sea state occurrence when normalized using 500 bins in each direction.

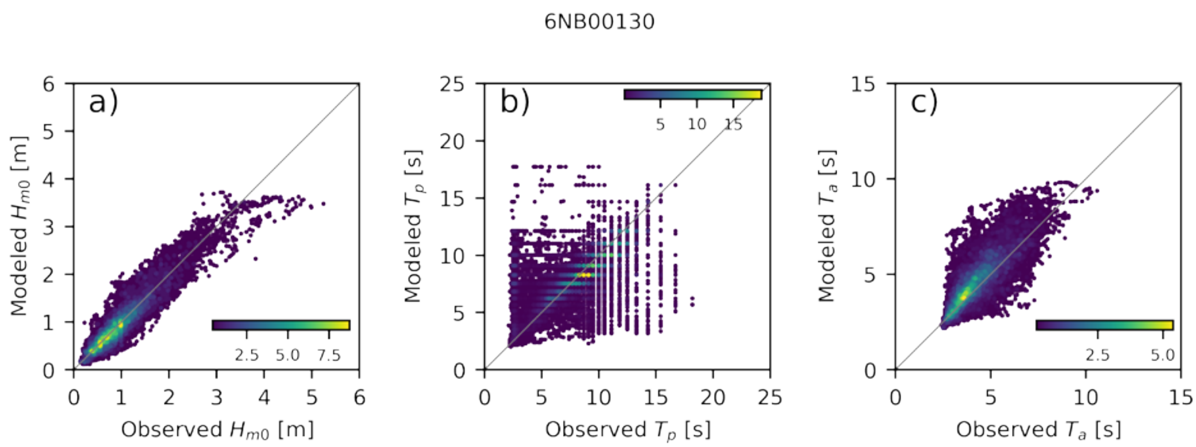

Figure 4.5. Same as Figure 4.4 for the New Jersey deployment.

To provide a quantitative assessment, model results were interpolated in time to the buoy measurements for the model–data comparisons. Significant wave height error statistics are shown in Table 4.1. The RMSE errors are comparable to those computed against altimetry data. The largest percent error (in absolute terms) was found at 44064 at the mouth of Chesapeake Bay because of the lack of estuarine circulation in the currents that were used to force the model. Outside of that location, all buoys show similar bias and errors, giving confidence in the model results at the shelf scale.

Table 4.1. Error statistics for significant wave height.

Buoy/Parameter	N	RMSE [m]	PE [%]	SI	Bias [m]	Bias [%]	R
6NB00120	38,553	0.24	7.4	0.20	0.06	5.0	0.93
6NB00130	32,445	0.18	0.0	0.18	−0.01	−1.4	0.93
41025	30,788	0.39	15.7	0.26	0.19	12.9	0.91
44009	28,349	0.28	15.9	0.24	0.14	12.0	0.94
44014	34,119	0.35	18.0	0.24	0.19	13.2	0.94
44025	27,861	0.32	16.6	0.25	0.17	12.7	0.93
44064	25,538	0.22	−28.1	0.37	−0.17	−27.3	0.90
44065	28,060	0.21	5.0	0.20	0.03	2.7	0.93
44066	27,111	0.41	19.3	0.25	0.23	14.2	0.94
44089	24,576	0.19	0.9	0.19	0.00	−0.3	0.92
44091	45,734	0.24	3.5	0.19	0.03	2.1	0.94
44093	41,628	0.22	2.1	0.18	0.01	0.5	0.93
44095	58,104	0.25	5.9	0.19	0.04	2.7	0.94
44096	55,391	0.20	−8.8	0.21	−0.09	−9.7	0.93
44099	67,336	0.19	−1.2	0.18	−0.01	−1.3	0.94
44100	52,704	0.23	−2.0	0.19	−0.06	−4.7	0.95

N is the number of observations; PE is percentage error; R is the linear correlation coefficient; SI is scatter index

In addition to total energy (i.e., significant wave height), buoys also provide spectral information that current altimeter technology cannot measure, thus enabling comparisons of periods and directions. Error statistics for T_p and T_a are shown in Table 4.2 and Table 4.3, respectively. As anticipated by the scatter comparisons, T_a is predicted with higher skill than T_p.

Table 4.2. Same as Table 4.1 but for peak wave period.

Buoy/Parameter	N	RMSE [s]	PE [%]	SI	Bias [s]	Bias [%]	R
6NB00120	38,553	1.98	9.3	0.27	0.12	1.7	0.63
6NB00130	32,445	2.60	20.6	0.34	0.30	4.0	0.59
41025	30,788	1.85	4.2	0.23	−0.01	−0.2	0.65
44009	28,349	1.99	5.1	0.26	−0.05	−0.6	0.65
44014	34,119	1.79	5.2	0.23	0.10	1.2	0.68
44025	27,861	1.97	6.4	0.27	0.06	0.8	0.64
44064	25,538	3.80	65.8	1.03	2.45	66.4	0.50
44065	28,060	2.27	7.7	0.30	−0.06	−0.8	0.61
44066	27,111	1.80	3.1	0.23	−0.06	−0.7	0.68
44089	24,576	2.69	2.1	0.33	−0.49	−6.1	0.57
44091	45,734	2.31	3.2	0.30	−0.27	−3.5	0.60
44093	41,628	1.98	1.5	0.26	−0.28	−3.6	0.64
44095	58,104	2.01	2.2	0.24	−0.19	−2.3	0.67
44096	55,391	2.54	−1.9	0.32	−0.68	−8.5	0.60
44099	67,336	2.26	1.3	0.29	−0.37	−4.7	0.63
44100	52,704	2.30	−0.1	0.28	−0.46	−5.5	0.61

Table 4.3. Same as Table 4.1 but for mean wave period.

Buoy/Parameter	N	RMSE [s]	PE [%]	SI	Bias [s]	Bias [%]	R
6NB00120	38,553	0.60	4.5	0.13	0.17	3.7	0.79
6NB00130	32,445	0.77	8.8	0.18	0.35	8.1	0.82
41025	30,788	0.72	−5.6	0.13	−0.35	−6.3	0.81
44009	28,349	0.69	−5.1	0.14	−0.28	−5.5	0.81
44014	34,119	0.62	−3.8	0.11	−0.23	−4.3	0.85
44025	27,861	0.66	−5.6	0.13	−0.31	−6.0	0.85
44064[1]	-	-	-	-	-	-	-
44065	28,060	0.74	−5.2	0.15	−0.28	−5.6	0.82
44066	27,111	0.68	−5.8	0.12	−0.34	−6.2	0.85
44089	24,576	0.87	−9.0	0.17	−0.51	−10.0	0.83
44091	45,734	0.79	−7.8	0.15	−0.45	−8.6	0.83
44093	41,628	0.79	−8.9	0.15	−0.50	−9.7	0.80
44095	58,104	0.83	−8.4	0.15	−0.51	−9.4	0.84
44096	55,391	0.96	−12.4	0.20	−0.65	−13.4	0.78
44099	67,336	0.81	−9.7	0.16	−0.51	−10.2	0.80
44100	52,704	0.99	−11.7	0.18	−0.68	−12.6	0.81

Error statistics at 44025 show comparable model performance to those found by Allandadi et al. (2019) for a Simulating WAves Nearshore (SWAN)-based hindcast. It is worth noting that the hindcast periods are different, and the purpose is to show the present model is aligned with similar efforts in the region.

4.3 Buoy-based Comparison: Wave Direction

The characterization of the model performance for wave direction is performed separately because directions are periodic, where 0° and 360° have the same meaning. Qualitatively, the model reproduces the evolution of the directional wave spectra. Figure 4.6 shows the mean wave direction for a period of three months where both buoys were deployed. The direction convention used in this section is the direction waves are coming from, measured clockwise from true North. If waves are traveling from the east to the west the direction will be 90°.

[1] 44064 did not report mean period data.

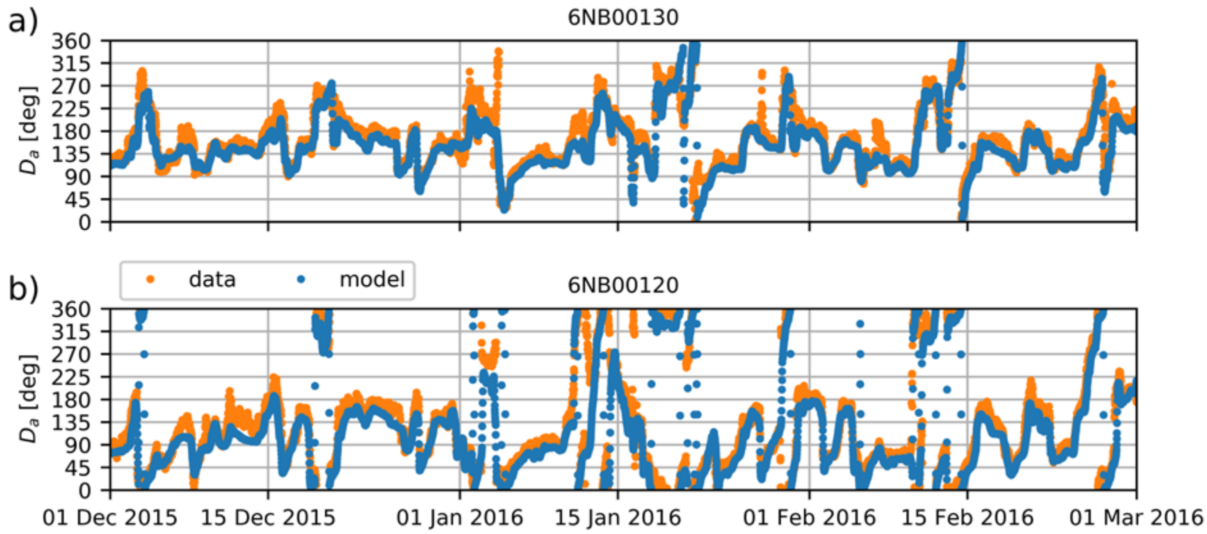

Figure 4.6. Mean wave direction time series at the (a) New Jersey and (b) Virginia deployments for a 3-month period.

Wave roses of D_a over the deployment period are shown in Figure 4.7 and colored by H_{m0} occurrence. Model results are interpolated to measurements; therefore, the same number of data points are included in each row. Data are binned every 22.5°. The general trend of the observations is qualitatively captured by the model hindcast. At the New Jersey deployment, the model underpredicts the number of waves approaching from the south-southwest correctly. For the Virginia deployment (bottom row) the principal direction of propagation (from the east-northeast) is correctly captured. Overall, the model appears smoother (i.e., all bars have similar lengths) than the measurements.

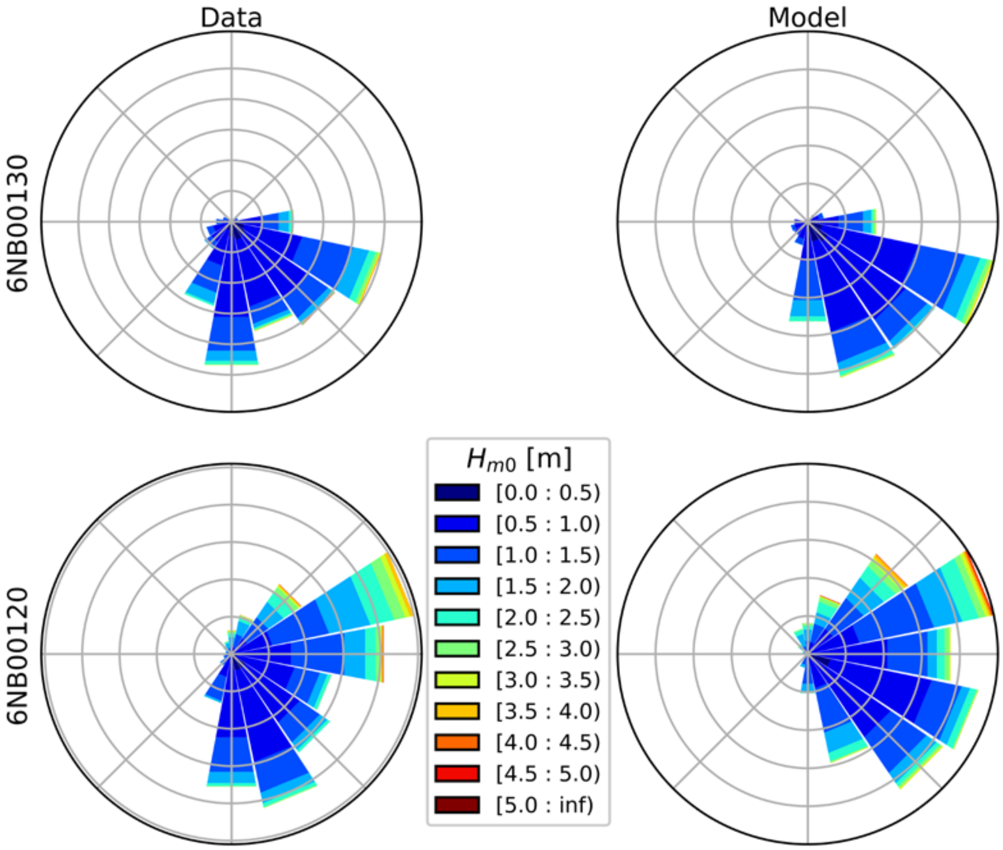

Figure 4.7. Wave roses based on vector mean wave direction from (*left*) measurements and (*right*) the model. The radial dimension of each row is constant.

Besides capturing the mean wave direction, the model must be able to simulate bimodal seas and the distribution of the energy correctly. As an example, instantaneous wave spectra are shown in Figure 4.8. During this time, the wave field is unimodal at the New Jersey deployment location. The model is able to reproduce the behavior, although the energy spread around the peak appears wider in the model than in the observations. At the same time, the sea state is bimodal in Virginia. Waves with a dominant period of ~10 s are approaching from the south east, while shorter 5 s waves are approaching from the north. The model qualitatively reproduces the sea state correctly.

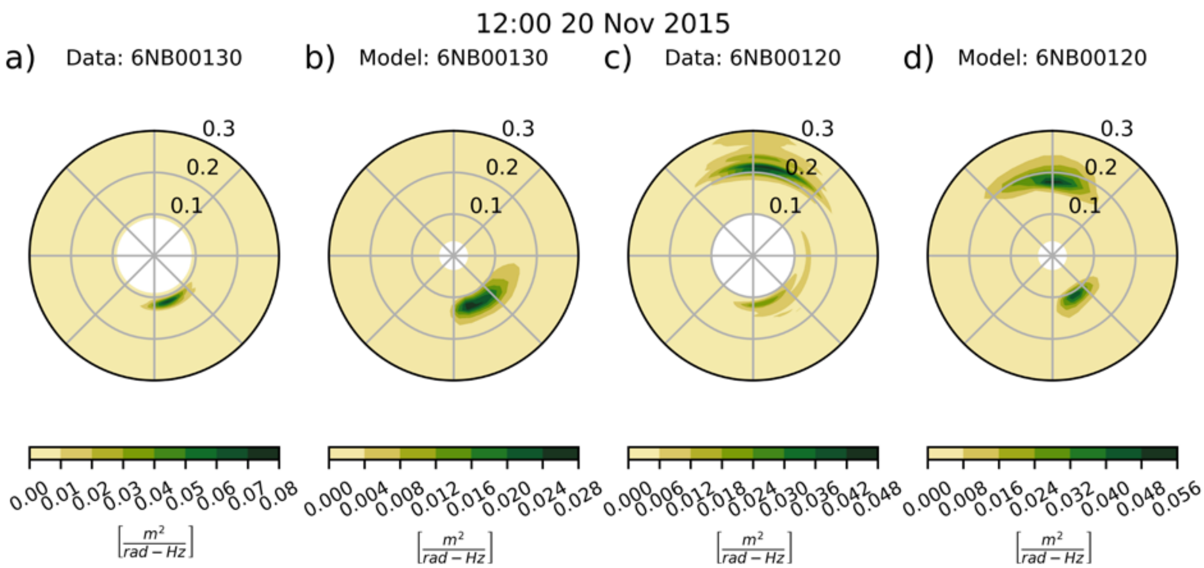

Figure 4.8. (a, c) Measured and (b, d) modeled wave spectra. The model directional resolution is 10°, and the measured data has been binned every 3°; thus the color scales will not necessarily match because the spectra have not been normalized. Radial contours at 0.1, 0.2, and 0.3 Hz.

Two error statistics were computed to quantify the directional model performance following the methodology of Hanson and Phillips (2001). The angular bias (Bowers et al. 2000):

$$Bias_\theta = \tan^{-1}\frac{\sum_{i=1}^{N}\sin\left|P_i - M_i\right|}{\sum_{i=1}^{N}\cos\left|P_i - M_i\right|} \tag{4.1}$$

where the variables *P* and *M* represent predicted and measured directions, respectively. A signed inverse tangent function is used, and the results are provided in the 0°–360° range. The circular correlation (Tracy 2002) is also considered:

$$R_\theta = \frac{\sum_{i=1}^{N}\sin\left(M_i - \bar{M}\right)\sin\left(P_i - \bar{P}\right)}{\sqrt{\sum_{i=1}^{N}\left(\sin\left(M_i - \bar{M}\right)\right)^2\sum_{i=1}^{N}\left(\sin\left(P_i - \bar{P}\right)\right)^2}} \tag{4.2}$$

where the overlines represent the average measurement.

These error statistics were computed for D_m and D_p and shown in Table 4.4. In general, the $bias_\theta$ is in the order of 10°–20° and R_θ above 0.80. These results should be interpreted in the context of the model directional resolution (10°) and the buoy measurement accuracy. NDBC[1] reports directional accuracy of ±10°. The model is less skillful in predicting D_p. This is not unexpected because D_p is computed as a discrete value that is not energy weighted, where errors in bimodal seas can be large if both peaks are of equal energy. Nonetheless, the model predicts the peak wave direction with 20° accuracy.

[1] https://www.ndbc.noaa.gov/rsa.shtml (retrieved 23 March 2020).

Table 4.4. Error statistics for mean and peak wave direction.

Buoy/Parameter	N	Mean Wave Direction Bias$_\theta$ [deg]	Mean Wave Direction R$_\theta$	Peak Wave Direction Bias$_\theta$ [deg]	Peak Wave Direction R$_\theta$
6NB00120	30,067	21	0.89	18	0.79
6NB00130	28,646	18	0.90	20	0.74
41025	30,751	16	0.87	23	0.71
44009	28,342	12	0.81	16	0.70
44014	34,119	13	0.87	18	0.71
44025	27,865	14	0.84	21	0.67
44064	-	-	-	-	-
44065	28,067	14	0.81	21	0.63
44066	27,069	13	0.83	20	0.65
44089	24,562	14	0.91	18	0.76
44091	45,736	13	0.90	19	0.71
44093	41,628	11	0.92	17	0.80
44095	58,104	12	0.93	17	0.82
44096	55,398	13	0.90	19	0.77
44099	67,343	11	0.91	17	0.79
44100	52,704	11	0.93	16	0.81

The mean in Equation (4.2) influences the correlations by a few decimal points. If the mean is fixed at 0°, R$_\theta$ for 6NB00120 and 6NB00130 is 0.87 and 0.88, respectively; if the correlations are fixed at 90°, R$_\theta$ is 0.86 and 0.93 for the same buoys, respectively.

4.4 Model Performance during Large Wave Events

Two named hurricanes of the 2016 Atlantic hurricane season, Hermine and Matthew, affected the Mid-Atlantic Bight during the Lidar buoy deployments. The former brought larger waves than the latter. In addition, many Nor'easters affected the area, of which the January 2016 event brought the largest waves recorded by the buoys. The model performance during two of these events is evaluated in this section.

4.4.1 January 2016 Winter Storm

A powerful winter storm rated Category 4 by the National Oceanic and Atmospheric Administration impacted the region between 22–24 January 2016. The largest wave heights measured by the Lidar buoys occurred during this event. During model development, this storm was used as part of the model calibration (Shaw et al. 2020). The results are shown here for verification and analysis.

The significant wave height measured at the Lidar buoys exceeded 5 m and had dominant periods in the order of 10 s (Figure 4.9). Farther offshore, waves reached H_{m0} of 9 m, as measured by the HY-2 altimeter. During this event, the wave model captured the H_{m0} peaks to within less than a meter at the Lidar buoys. This is not unexpected because the calibration was performed at the buoys. However, the model shows good performance when compared to the altimeters, where wave heights were being predicted accurately to within 50 cm.

Local wave growth because of strong winds can be deduced from the sharp increase in energy transferred from the atmosphere to the waves seen in integrated form (Figure 4.10c). Wave growth is balanced by dissipation due to whitecapping (Figure 4.10d), but the magnitude of the dissipation was less than the input during the event. A snapshot of wave spectra on 23 January 2016 shows the spectra is unimodal at the New Jersey deployment, while a bimodal spectrum was captured at the Virginia site (Figure 4.11). The high-frequency spectral peak at the Virginia site is correlated with the local wind forcing, which has a northerly direction (Figure 4.11). The instantaneous source term balance [right-hand side of Equation (2.1)] shows net gain of energy.

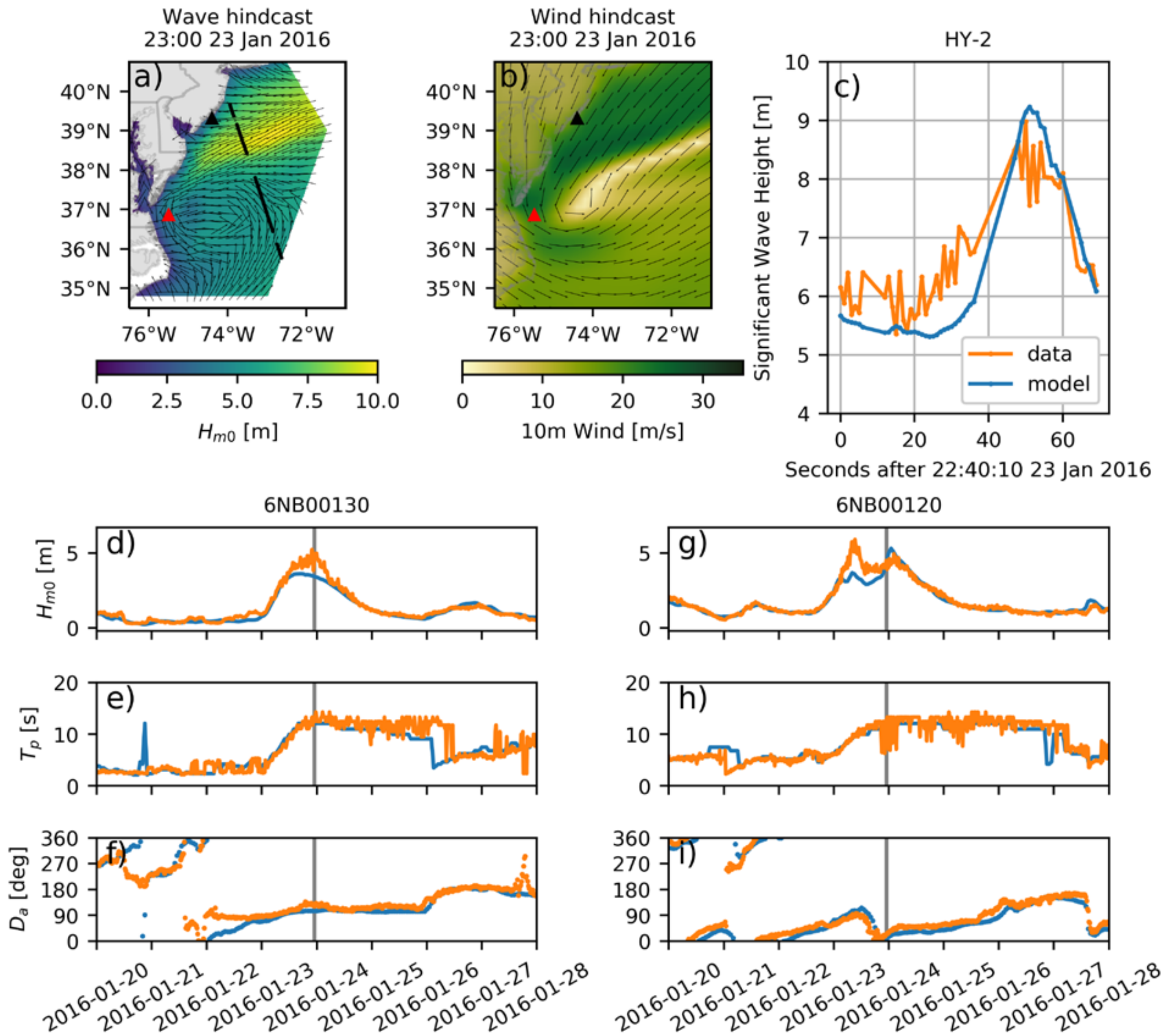

Figure 4.9. January 2016 blizzard model results. (a) Significant wave height and peak direction. (b) Wind speed and direction. (c) Model–data comparisons with HY-2 data. (d, g) Time series of significant wave height, (e,h) peak wave period, and (f,i) peak wave direction for the New Jersey (left) and Virginia (right) deployments.

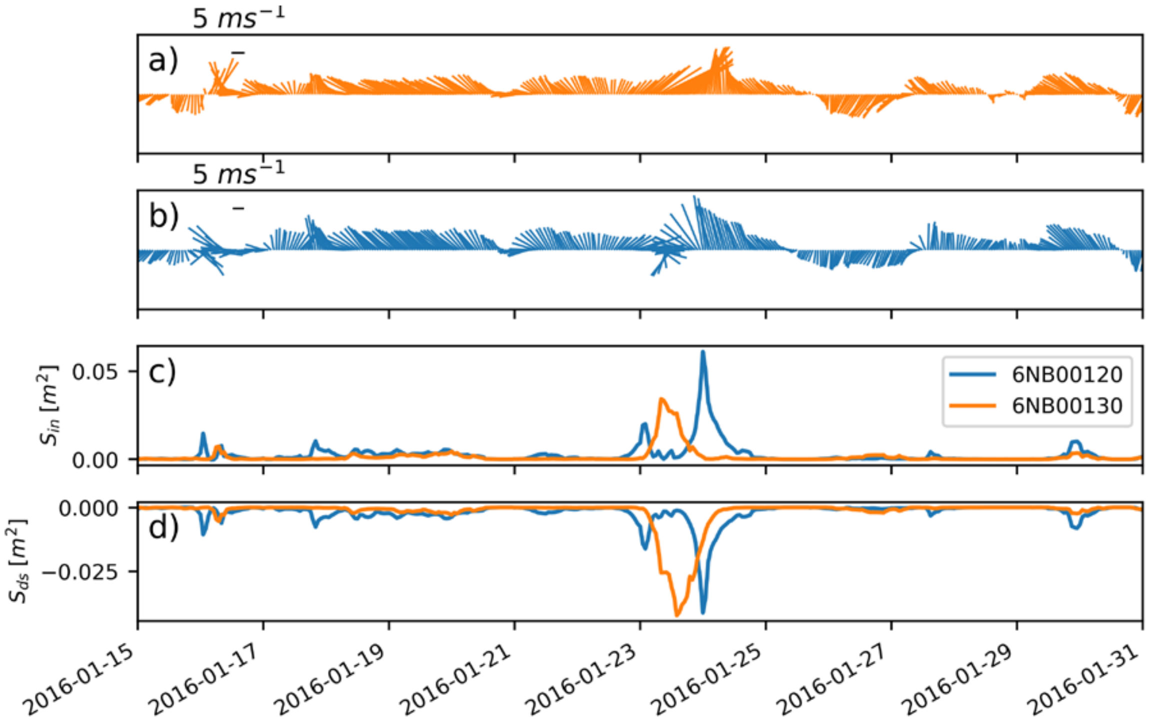

Figure 4.10. CFSRv2 derived 10 m wind speed for the (a) Virginia (6NB00120) and (b) New Jersey (6NB00130) deployments. (c) Wind input and dissipation due to whitecapping (d) source terms.

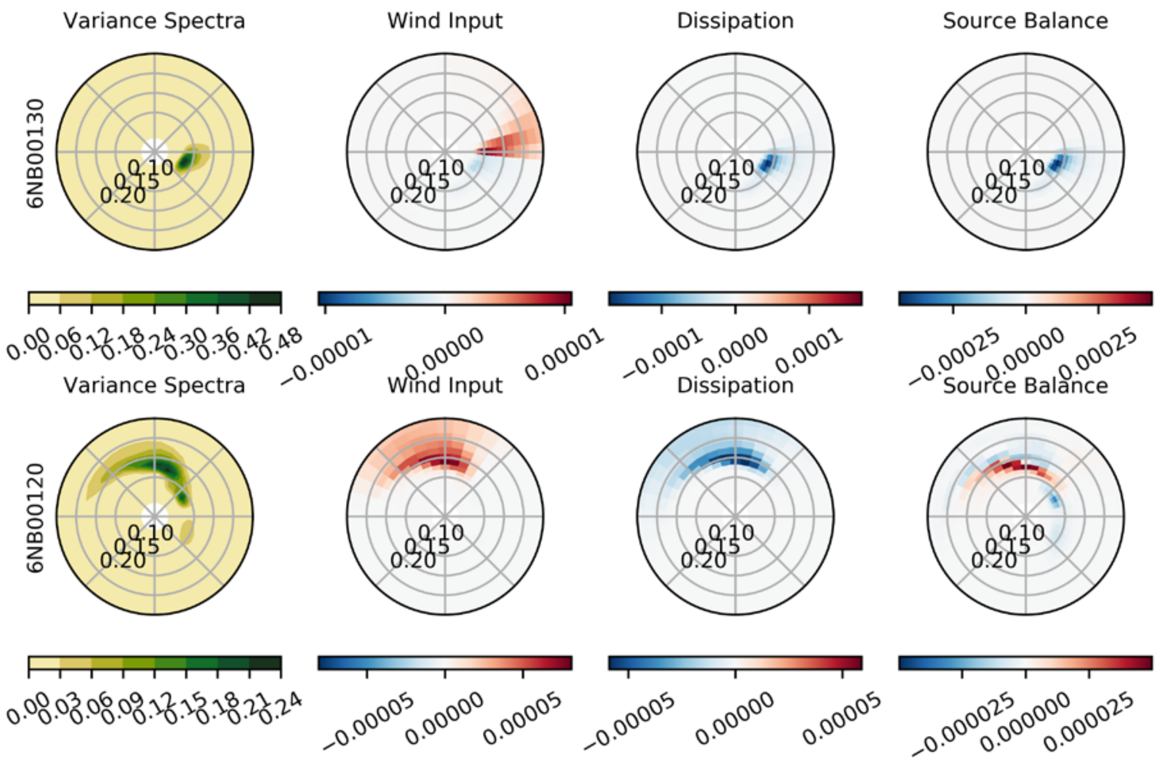

Figure 4.11. Frequency and directionally resolved wave spectra and source term balance. Time is the same as Figure 4.6. Colormap units are m^2/Hz-rad.

4.4.2 Hurricane Hermine

Hurricane Hermine approached the North Carolina and Virginia coasts as a tropical storm on 3 September 2016. During this event, only the New Jersey buoy was active. To evaluate the model's performance at the site of the Virginia deployment, model–data comparisons were made for NDBC buoy 44093. Buoy 44093 was located 600 m from the Lidar buoy deployment location, which is a distance smaller than the model resolution. Figure 4.12 show the details of the event at the time of maximum measured wave height at 44093. The wave direction (Figure 4.12a) offshore of North Carolina and Virginia follows the same pattern as the wind forcing (Figure 4.12b). The Sentinel-3A altimeter provides a wave height track three hours before the model snapshots at the offshore end of the domain. WW3 overpredicts the small wave heights offshore for this event but is able to capture the larger waves in the event (Figure 4.12c). However, over the inner shelf at the buoy locations, the model performs very well for wave height (Figure 4.12d,g), peak period (Figure 4.12d,h), and direction (Figure 4.12f,i).

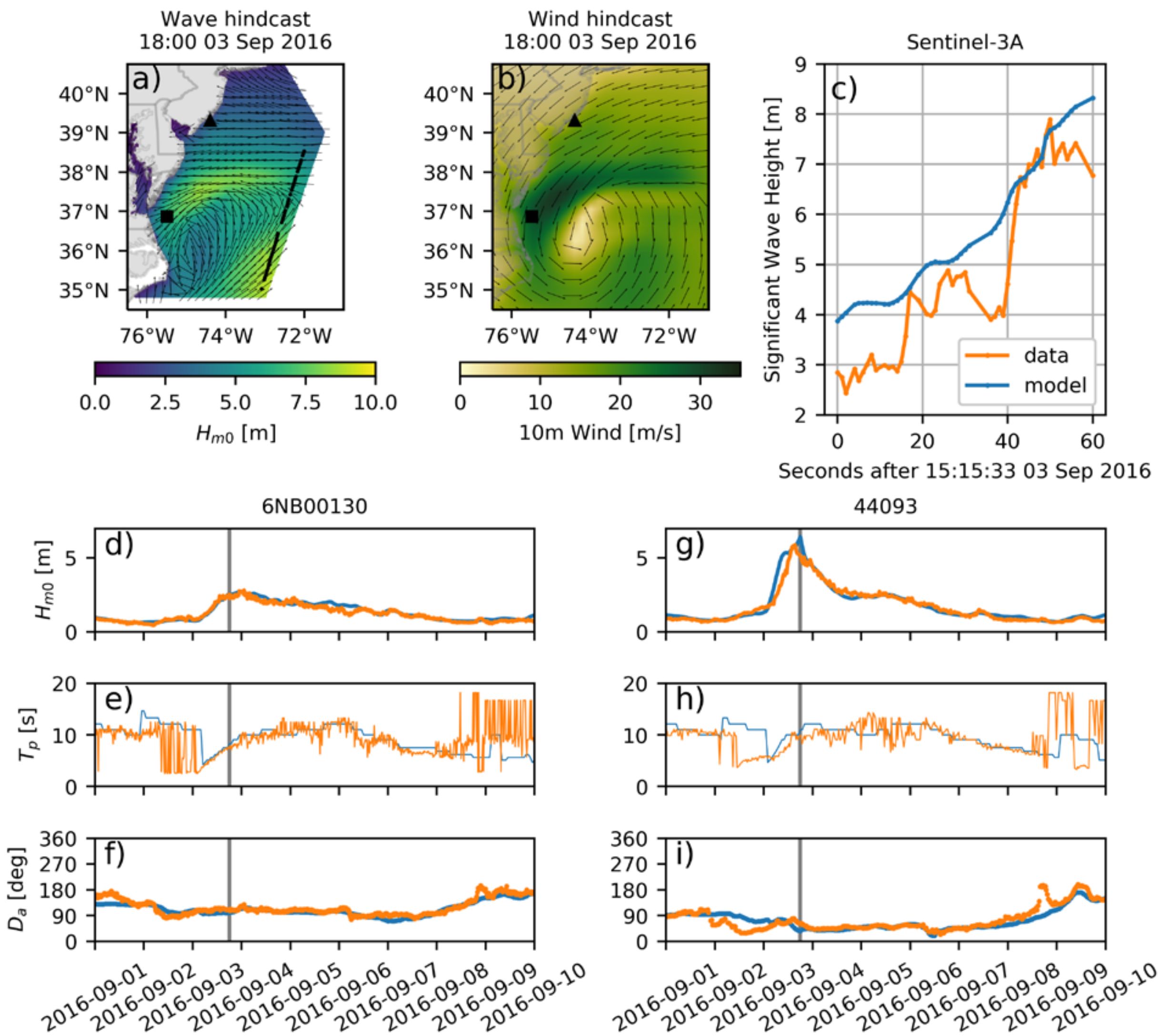

Figure 4.12. Same as Figure 4-9 but pertaining to Hurricane Hermine. (c) Altimetry comparisons are made with Sentinel-3A and time series for 44093.

Both locations have unimodal spectra (Figure 4.13) that are actively forced by wind. Forcing offshore of Virginia is an order of magnitude larger than near New Jersey, as can be inferred from the instantaneous wind patterns in Figure 4.12b. In fact, the source term balance shows that dissipation dominates over wind input at the New Jersey site.

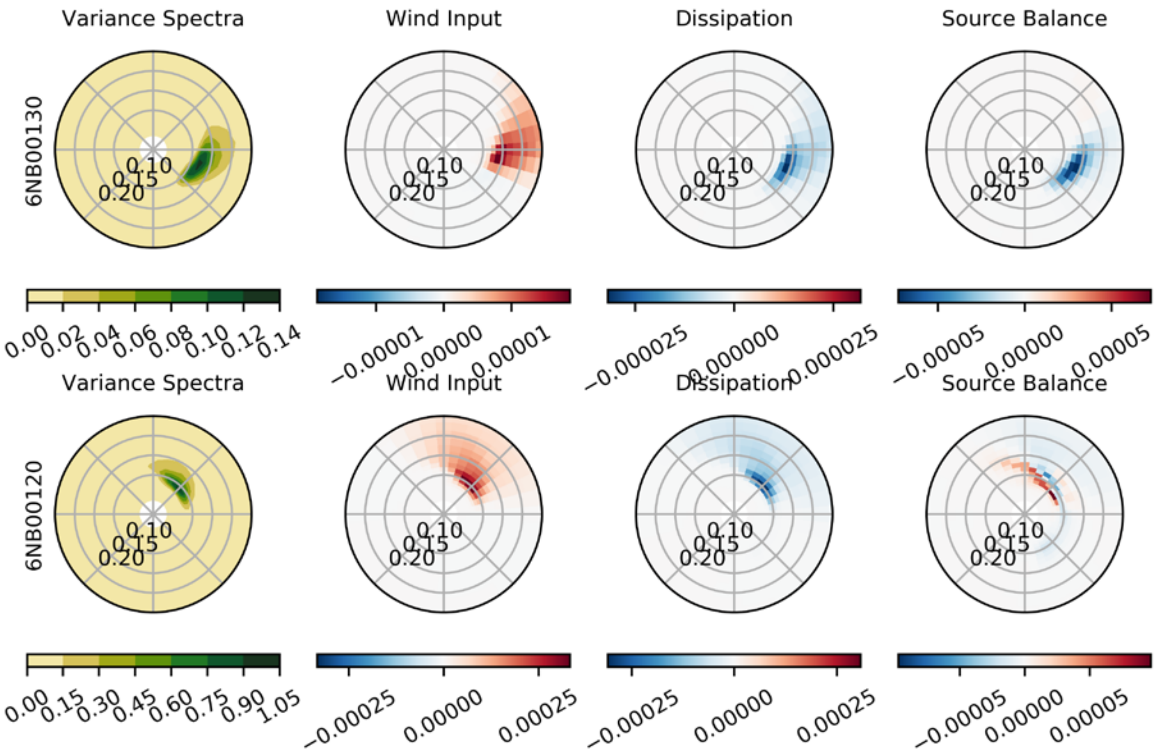

Figure 4.13. Same as Figure 4.11 for 3 September 2016 at 18:00 UTC.

5.0 Stored Model Output

Integrated wave parameters were stored at each grid point at hourly intervals. They include the directionality coefficient, mean wave direction, peak wave direction, direction of maximum directionally resolved wave power, peak frequency, significant wave height, omnidirectional wave power, directional spread, mean wave, and mean wave period. Wave spectra and source terms are stored at hourly intervals at the ground truth stations, the Lidar buoys, and at lines of equal distance from shore, as shown in Figure 5.1. The latter points are stored at 5, 10, 15, 20, 25, 30, 40, 50, 60, 70, 80, 90, 100, 110, 130, 150, 170, and 190 km from the main shoreline.

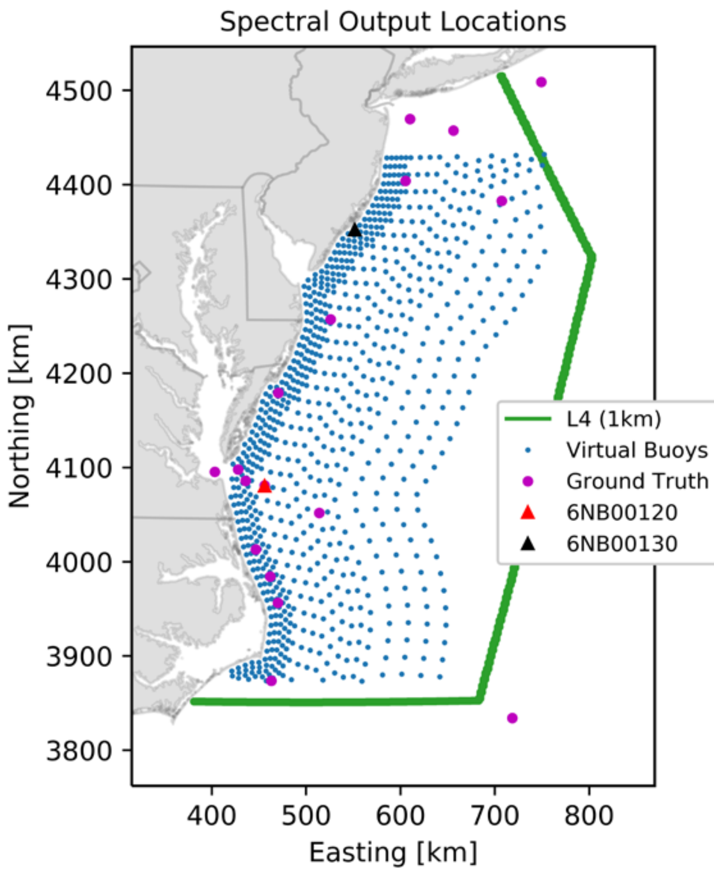

Figure 5.1. Spectral and source term output locations.

6.0 Summary

This report summarizes the model validation and results from a 4-year (2014–2017) wave hindcast in the Mid-Atlantic Bight. The purpose of the wave model is to supplement the Lidar buoy measurements with the aim of improving lower boundary characterization for atmospheric models. The wave model was developed based on WW3 at a spatial resolution of approximately 2 km. The modeling system contained four levels of models to dynamically downscale the waves to the shelf scale. Wind and ocean surface currents were obtained from CFSRv2 and HYCOM, respectively, to drive the wave model.

The model was validated against satellite altimetry and buoy measurements and shows good accuracy, with RMSE errors in significant wave height in the order of 20–40 cm. Periods were predicted with less accuracy but within the range of published values. The model also predicted large wave events, due to hurricanes and Nor'easters, accurately. Wave spectra and source terms were stored at the Lidar buoy locations and at 829 virtual stations at lines of equal distance from shore.

7.0 References

Allandadi MN, B Gunawan, J Lai, RY He and VS Neary. 2019. "Development and validation of a regional-scale high-resolution unstructured model for wave energy resource characterization along the US East Coast." *Renewable Energy* 136:500-511. DOI: http://dx.doi.org/10.1016/j.renene.2019.01.020.

Bowers JA, ID Morton and GI Mould. 2000. "Directional statistics of the wind and waves." *Applied Ocean Research* 22(1):13-30. DOI: http://dx.doi.org/10.1016/S0141-1187(99)00025-5.

Carter DJT, PG Challenor and MA Srokosz. 1992. "An Assessment of Geosat Wave Height and Wind-Speed Measurements." *Journal of Geophysical Research-Oceans* 97(C7):11383-11392. DOI: http://dx.doi.org/10.1029/92jc00465.

Drennan WM, KK Kahma and MA Donelan. 1999. "On momentum flux and velocity spectra over waves." *Boundary-Layer Meteorology* 92(3):489-515. DOI: http://dx.doi.org/10.1023/A:1002054820455.

Drennan WM, PK Taylor and MJ Yelland. 2005. "Parameterizing the sea surface roughness." *Journal of Physical Oceanography* 35(5):835-848. DOI: http://dx.doi.org/10.1175/Jpo2704.1.

García-Medina G, HT Özkan-Haller and P Ruggiero. 2014. "Wave resource assessment in Oregon and southwest Washington, USA." *Renewable Energy* 64:203-214. DOI: http://dx.doi.org/10.1016/j.renene.2013.11.014.

García-Medina G, HT Özkan-Haller, P Ruggiero and J Oskamp. 2013. "An Inner-Shelf Wave Forecasting System for the U.S. Pacific Northwest." *Weather and Forecasting* 28(3):681-703. DOI: http://dx.doi.org/10.1175/waf-d-12-00055.1.

Grachev AA and CW Fairall. 2001. "Upward momentum transfer in the marine boundary layer." *Journal of Physical Oceanography* 31(7):1698-1711. DOI: http://dx.doi.org/10.1175/1520-0485(2001)031<1698:Umtitm>2.0.Co;2.

Halliwell GR. 2004. "Evaluation of Vertical Coordinate and Vertical Mixing Algorithms in the HYbrid-Coordinate Ocean Model (HYCOM)." *Ocean Modelling* 7(3-4):285-322. DOI: http://dx.doi.org/10.1016/j.ocemod.2003.10.002.

Hanson JL and OM Phillips. 2001. "Automated analysis of ocean surface directional wave spectra." *Journal of Atmospheric and Oceanic Technology* 18(2):277-293. DOI: http://dx.doi.org/10.1175/1520-0426(2001)018<0277:Aaoosd>2.0.Co;2.

Kuik AJ, GP Vanvledder and LH Holthuijsen. 1988. "A Method for the Routine Analysis of Pitch-and-Roll Buoy Wave Data." *Journal of Physical Oceanography* 18(7):1020-1034. DOI: http://dx.doi.org/10.1175/1520-0485(1988)018<1020:Amftra>2.0.Co;2.

Longuet-Higgins MS, DE Cartwright and ND Smith. 1963. "Observations of the directional spectrum of sea waves using the motion of a floating body." In *Ocean Wave Spectra*, pp. 111-136. Englewood Cliffs, NJ: Prentice-Hall.

Nwogu O, E Mansard, M Miles and M Isaacson. 1987. "Estimation of directional wave spectra by the maximum entropy method." In *Proc. IAHR Seminar on Wave Analysis and Generation in Laboratory Basins, 22nd IAHR Congress*, pp. 363-376 Lausanne, Switzerland.

Pan JY, DW Wang and PA Hwang. 2005. "A study of wave effects on wind stress over the ocean in a fetch-limited case." *Journal of Geophysical Research-Oceans* 110(C2). DOI: http://dx.doi.org/10.1029/2003jc002258.

Ribal A and IR Young. 2019. "33 years of globally calibrated wave height and wind speed data based on altimeter observations." *Scientific Data* 6. DOI: http://dx.doi.org/10.1038/s41597-019-0083-9.

Saha S, S Moorthi, XR Wu, J Wang, S Nadiga, P Tripp, D Behringer, YT Hou, HY Chuang, M Iredell, M Ek, J Meng, RQ Yang, MP Mendez, H Van Den Dool, Q Zhang, WQ Wang, MY Chen and E Becker. 2014. "The NCEP Climate Forecast System Version 2." *Journal of Climate* 27(6):2185-2208. DOI: http://dx.doi.org/10.1175/Jcli-D-12-00823.1.

Shaw WJ, J Draher, G García Medina, AM Gorton, R Krishnamurthy, RK Newsom, MS Pekour, LM Sheridian and Z Yang. 2020. *General Analysis of Data Collected from DOE Lidar Buoy Deployments Off Virginia and New Jersey*. PNNL-29823. Richland, WA: Pacific Northwest National Laboratory. Unpublished.

Shaw WJ, MS Pekour and RK Newsom. 2018. *Lidar Buoy Data Analysis: Basic Assessment of Observed Conditions and Instrument Performance Off Virginia and New Jersey*. PNNL-28058. Richland, WA, USA: Pacific Northwest National Laboratory. Available at https://www.osti.gov/servlets/purl/1481260.

Steele KE, CC Teng and DWC Wang. 1992. "Wave Direction Measurements Using Pitch-Roll Buoys." *Ocean Engineering* 19(4):349-375. DOI: http://dx.doi.org/10.1016/0029-8018(92)90035-3.

Taylor PK and MJ Yelland. 2001. "The dependence of sea surface roughness on the height and steepness of the waves." *Journal of Physical Oceanography* 31(2):572-590. DOI: http://dx.doi.org/10.1175/1520-0485(2001)031<0572:Tdossr>2.0.Co;2.

Tolman HL and WAVEWATCH III Development Group. 2014. *User manual and system documentation of WAVEWATCH III® version 4.18*. College Park, MD: National Oceanic and Atmospheric Administration, National Weather Service, National Centers for Environmental Prediction.

Tracy BA. 2002. "Directional Characteristics of the 1990-1999 Wave Information Studies Gulf of Mexico Hindcast." In *Seventh International Workshop on Wave Hindcasting and Forecasting*, p. 10. October 21-25, 2002, Banff, Alberta, Canada.

Wu W-C, Z Yang and T Wang. 2018. "Wave Resource Characterization Using an Unstructured Grid Modeling Approach." *Energies* 11(3):15. DOI: http://dx.doi.org/10.3390/en11030605.

Yang Z, VS Neary, T Wang, B Gunawan, AR Dallman and W Wu. 2017. "A wave model test bed study for wave energy resource characterization." *Renewable Energy* 114:132-144. DOI: http://dx.doi.org/10.1016/j.renene.2016.12.057.

Young IR and MA Donelan. 2018. "On the Determination of Global Ocean Wind and Wave Climate from Satellite Observations." *Remote Sensing of Environment* 215:228-241. DOI: http://dx.doi.org/10.1016/j.rse.2018.06.006.

Appendix A – Model Performance Metrics

The following performance metrics used in previous studies (García-Medina et al. 2013; García-Medina et al. 2014; Yang et al. 2017; Wu et al. 2018) were adopted here for model validation:

The root-mean-square error (*RMSE*):

$$RMSE = \sqrt{\frac{\sum_{i=1}^{N}\left(P_i - M_i\right)^2}{N}}, \qquad \text{(A.1)}$$

where N is the number of observations, M_i is the measured value, and P_i is the predicted value. *RMSE* represents the sample standard deviation of the differences between predicted and measured values. The percentage error (*PE*) is defined as:

$$PE\left(\%\right) = \frac{100}{N}\sum_{i=1}^{N}\left(\frac{P_i - M_i}{M_i}\right) \qquad \text{(A.2)}$$

which is the average over the period of comparison.

The scatter index (*SI*) is the *RMSE* normalized by the average of all measured values over the period of comparison, where

$$SI = \frac{RMSE}{\bar{M}}, \qquad \text{(A.3)}$$

where the overbar indicates the mean of the measured values.

Model bias, which represents the average difference between the predicted and measured value, is defined as

$$Bias = \frac{1}{N}\sum_{i=1}^{N}\left(P_i - M_i\right). \qquad \text{(A.4)}$$

Percentage bias is defined as

$$Bias\left(\%\right) = \frac{\sum_{i=1}^{N}P_i - \sum_{i=1}^{N}M_i}{\sum_{i=1}^{N}M_i} \cdot 100 \qquad \text{(A.5)}$$

which is also the normalized bias.

The linear correlation coefficient, R , is defined as

$$R = \frac{\sum_{i=1}^{N}\left(M_i - \bar{M}\right)\left(P_i - \bar{P}\right)}{\sqrt{\left(\sum_{i=1}^{N}\left(M_i - \bar{M}\right)^2\right)\left(\sum_{i=1}^{N}\left(P_i - \bar{P}\right)^2\right)}} \tag{A.6}$$

and is a measure of the strength of the linear relationship between the predicted and measured values.

Appendix B – Wave Height and Period Scatter Plots

These figures show the scatter between the model predictions and the observations. The relative occurrence of the different sea states is shown in colors where the histograms used to create the figures had 500 bins for both observations and measurements.

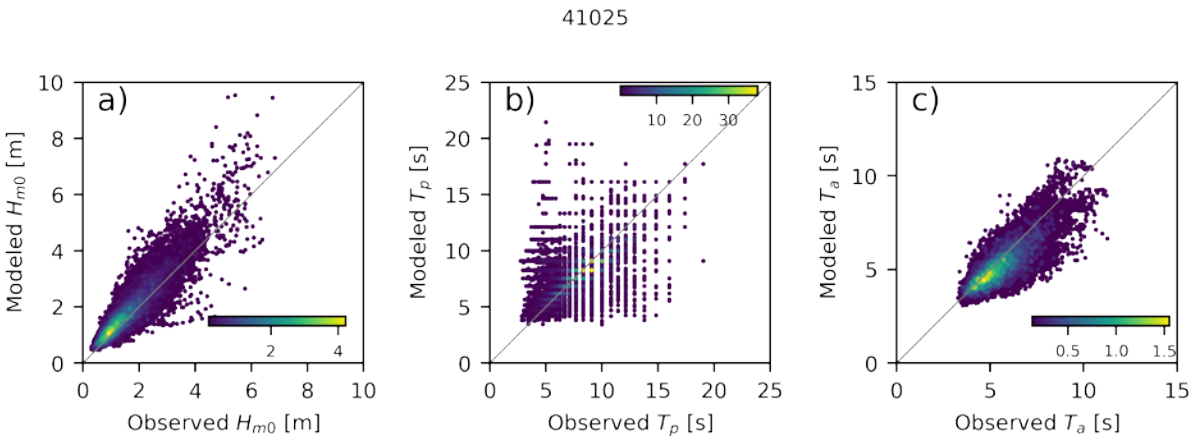

Figure B.1. Scatter plots for (a) significant wave height, (b) peak wave period, and (c) mean wave period for buoy 41025 between 2014 and 2017.

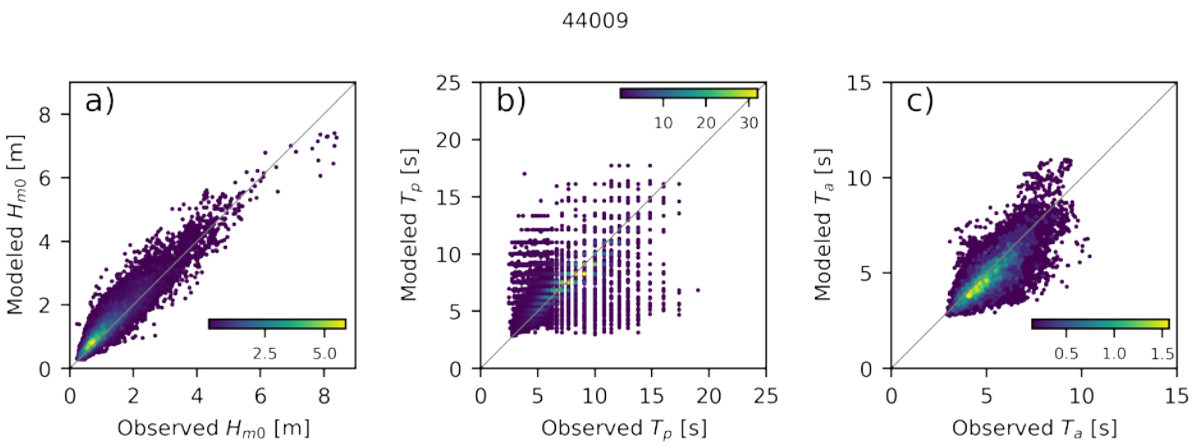

Figure B.2. Same as Figure B.1 for 44009.

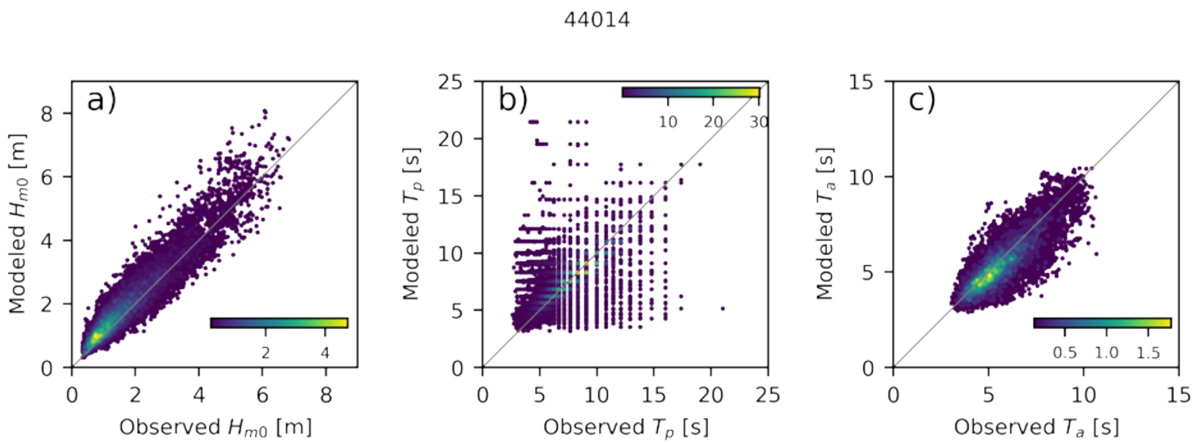

Figure B.3. Same as Figure B.1 for 44014.

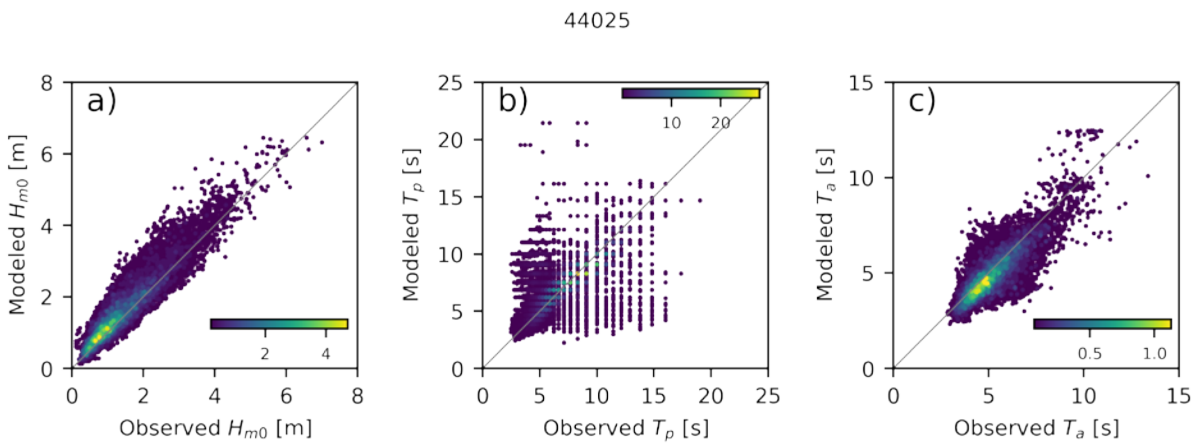

Figure B.4. Same as Figure B.1 for 44025.

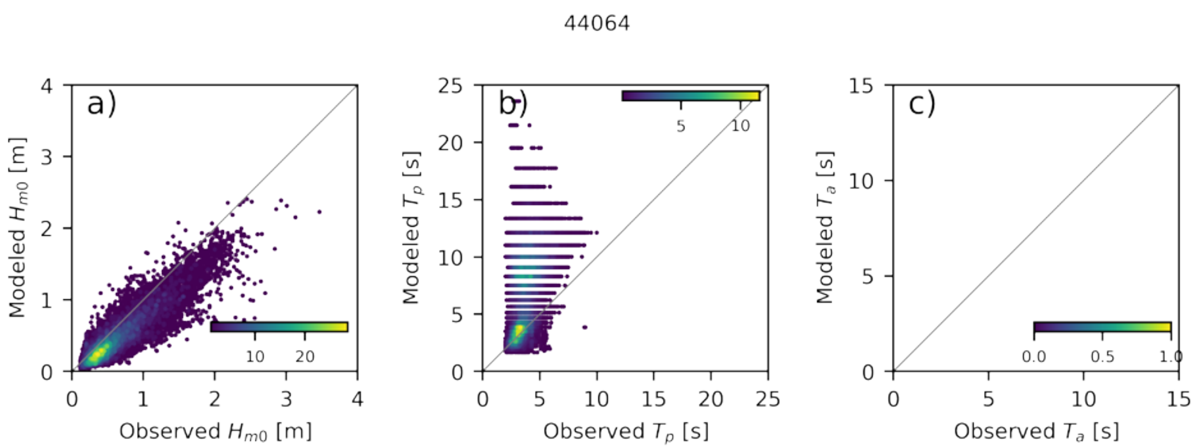

Figure B.5. Same as Figure B.1 for 44064.

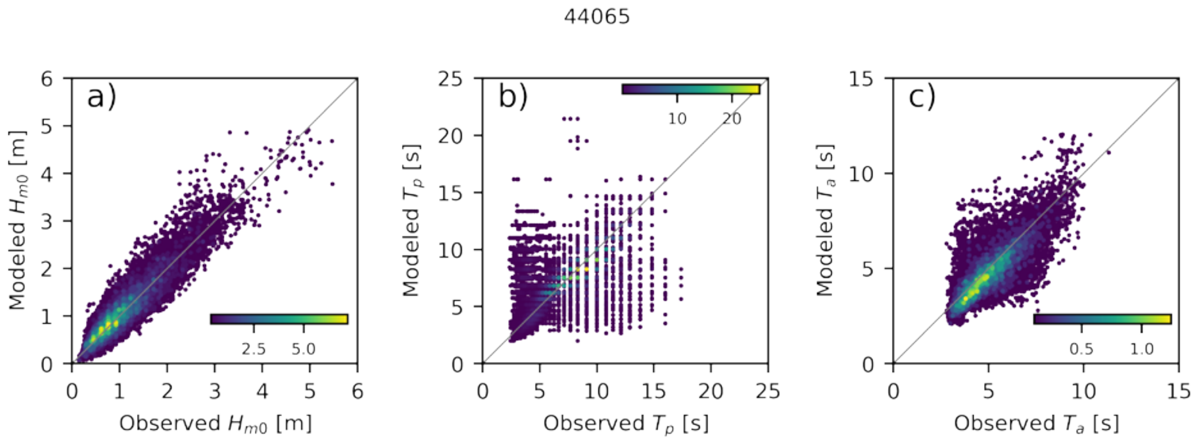

Figure B.6. Same as Figure B.1 for 44065.

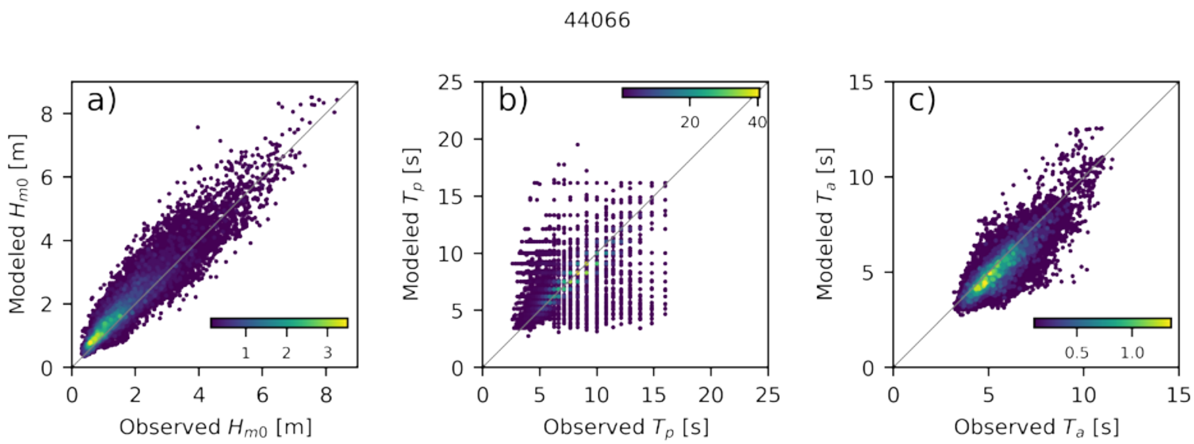

Figure B.7. Same as Figure B.1 for 44066.

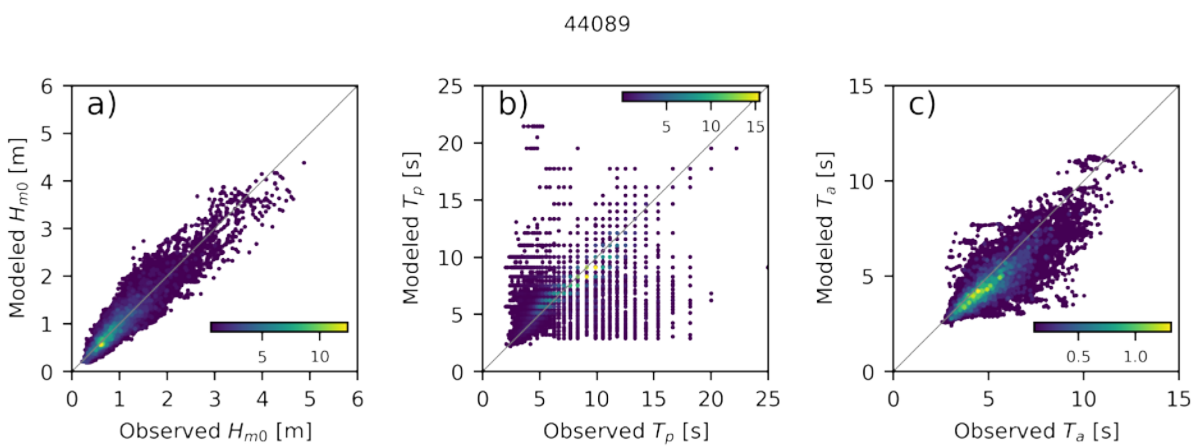

Figure B.8. Same as Figure B.1 for 44089.

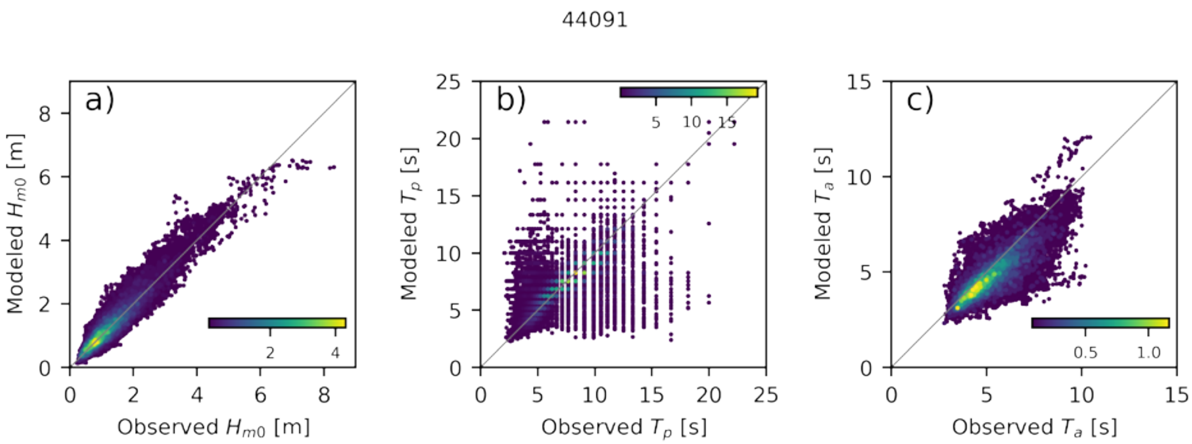

Figure B.9. Same as Figure B.1 for 44091.

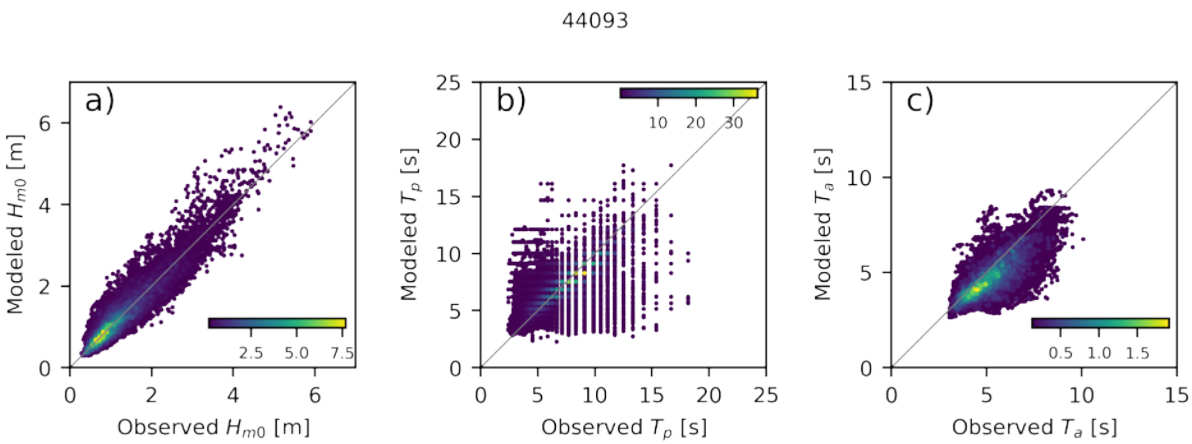

Figure B.10. Same as Figure B.1 for 44093.

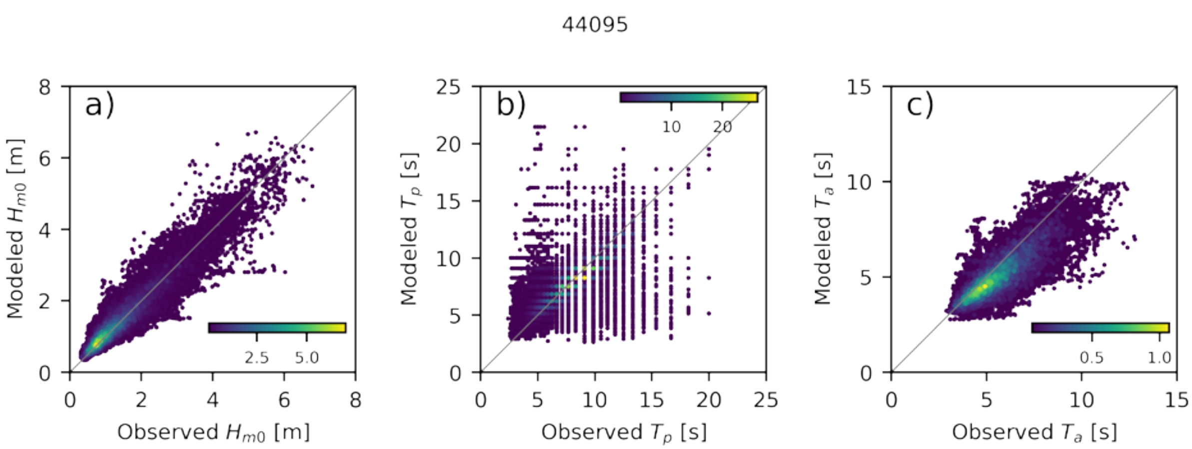

Figure B.11. Same as Figure B.1 for 44095.

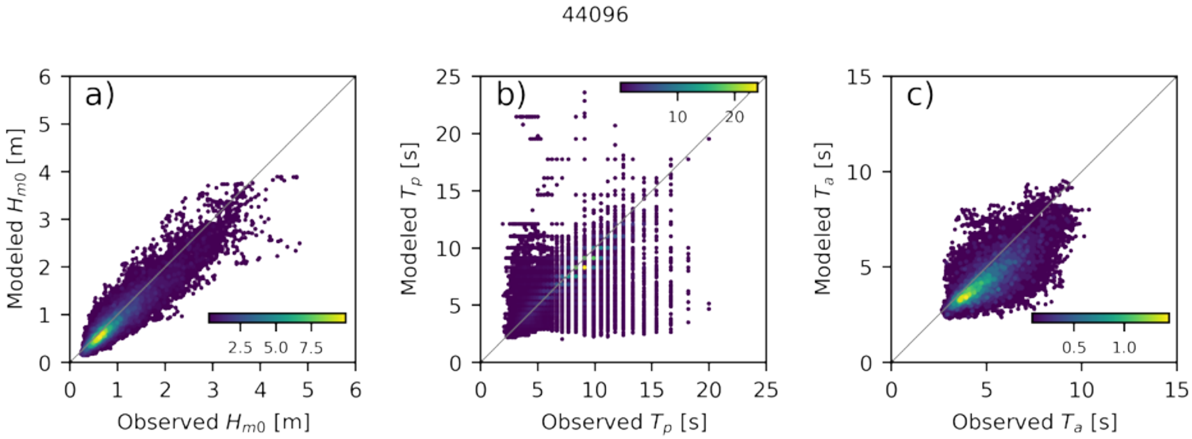

Figure B.12. Same as Figure B.1 for 44096.

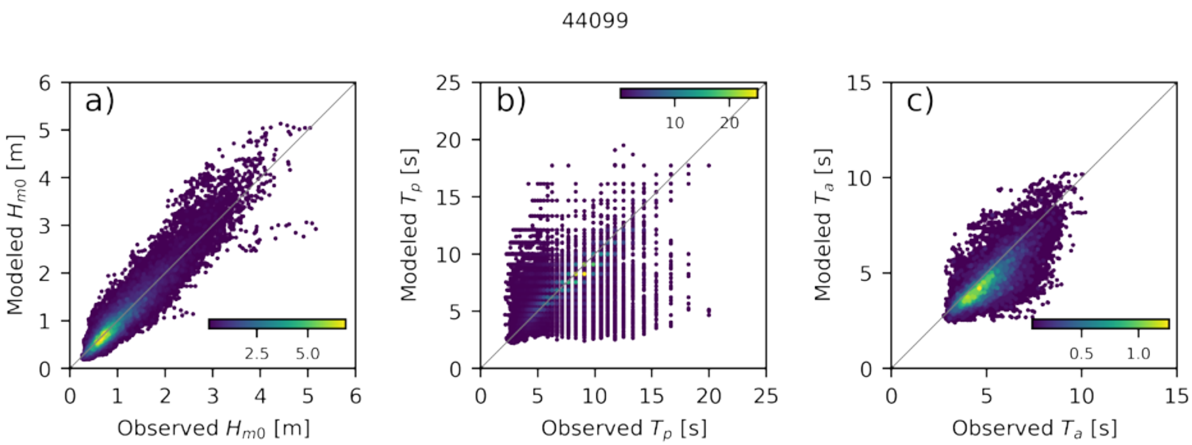

Figure B.13. Same as Figure B.1 for 44099.

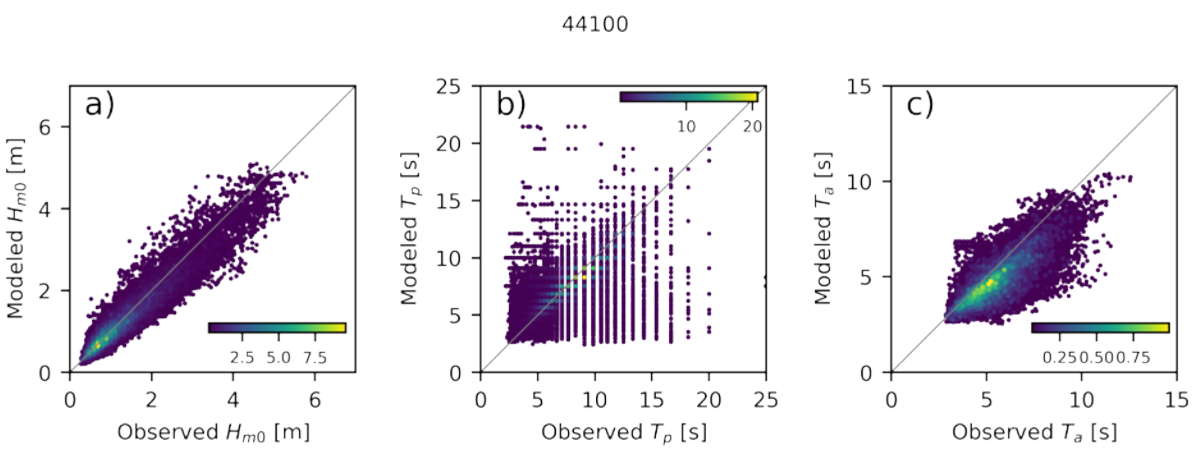

Figure B.14. Same as Figure B.1 for 44100.

Pacific Northwest National Laboratory

902 Battelle Boulevard
P.O. Box 999
Richland, WA 99354
1-888-375-PNNL (7665)

www.pnnl.gov